Brainwide genetic capture for conscious state transitions

Authors:
Hallie Lazaro[1,2*], Kevin N. Schneider[1,2,3*], Michelle Jin[4,5,6], Asad Beck[7], Daniel R. Rijsketic[8,9], Alexandria D. Murry[1,2,3], Jovana Navarrete[1,3,10], Cole C. Shin[1,2], Ainsley C. Barrow[1,2], Ian Campuzano[1,2], Minke H.C. Nota[1,2], Nick Ressler[1,3], Ella Apley[1,2], Jason Zhang[1,2], Glorianna Gutierrez[7], Eric R. Szelenyi[1,3], Simon RO Nilsson[11], Christine A. Denny[4,12], Michael R. Bruchas[1,2,13], Boris D. Heifets[8,14], Horacio O. de la Iglesia[7], Sam A. Golden[1,2,3†] and Mitra Heshmati[1,2,3†]

*These authors contributed equally to this work
†Co-senior authors
Correspondence to: mhesh@uw.edu

Affiliations:
[1] Center for Excellence in the Neurobiology of Addiction, Pain and Emotion, University of Washington, Seattle, WA
[2] Department of Anesthesiology and Pain Medicine, University of Washington, Seattle, WA
[3] Department of Neurobiology and Biophysics, University of Washington, Seattle, WA
[4] Department of Psychiatry, Columbia University Irving Medical Center, New York, NY
[5] Medical Scientist Training Program, Columbia University Irving Medical Center, New York, NY
[6] Doctoral Program in Neurobiology and Behavior, Columbia University, New York, NY
[7]Department of Biology, University of Washington, Seattle, WA
[8] Department of Anesthesiology, Perioperative, and Pain Medicine, Stanford University School of Medicine, Stanford, CA
[9] TensorAnalytics, Salt Lake City, UT
[10] Graduate Program in Neuroscience, University of Washington, Seattle, WA
[11] Platea Biosciences, Seattle, WA
[12] Division of Systems Neuroscience, Research Foundation for Mental Hygiene, Inc., New York State Psychiatric Institute, New York, NY
[13] Department of Pharmacology, University of Washington, Seattle, WA
[14] Department of Psychiatry and Behavioral Sciences, Stanford University School of Medicine, Stanford, CA

Acknowledgements:
This project was funded by the National Institute of General Medical Sciences R35GM146751 (to MH), a Foundation for Anesthesia Education and Research Mentored Research Training Grant (to MH), and a National Institute of Health Small Business Innovation Research Grant R44MH140096 (to SAG and MH). We also thank funding from the National Institute of Mental Health F31MH133295 (to JN), R01MH130591 (to BDH), the National Institute on Drug Abuse R37DA033396 (to MRB), P30DA048736 (to MRB), P50DA042012 (to BDH) and R01DA059374 (to SAG), the National Institute on Aging F30AG084312 (to MJ), the Washington Research Foundation (to ES and SAG), the University of Washington Anesthesiology & Perioperative Medicine Research Training grant T32GM086270 (to KNS). We thank Yizhe Zhang, Lukas MacMillen, Erica Sanchez, Andy Pelos, Rachael Hansen, and Dr. Kentaro Ishii for their technical

support. We thank Dr. Richard Palmiter for sharing Fos-2a-Cre transgenic mice and Dr. Cameron Good for supporting the mechano-acoustic device at NeuroLux, Inc. We also thank Dr. Nicholas Steinmetz and Dr. Zhiwen Ye for feedback on the high-density silicon probe studies.

Author Contributions: MH and SAG conceptualized and directed all aspects of the study. HL, ACB and MH performed activity-dependent chemogenetic behavioral experiments. HL and NR collected and analyzed mechano-acoustic recordings. HL, CCS, NR, EA, JZ, and SRON analyzed behavioral video recordings. KNS performed and analyzed high density silicon probe experiments. AB, GG and HOdlI performed electrocorticography recordings and analysis. MH, MRB and SAG designed whole brain studies. MJ and CAD performed network analysis. HL, JN, ADM, ACB, IC, MHCN, MH and SAG collected, cleared and imaged whole brain tissue. DRR, ADM, ES, IC, BDH, SAG and MH performed whole brain analysis. JN and ES prepared viruses and performed retroorbital virus injections. MH, SAG, HL, KNS and MJ wrote the first draft of the manuscript. All authors edited the manuscript.

Summary Abstract:

Spatially integrated mechanisms of consciousness are unclear[1,2]. An approach to manipulate brainwide circuits regulating consciousness via synthetic central nervous system activation may pave the way for more precise transitions in consciousness and reveal underlying mechanisms. Toward this goal, we leverage anesthesia as a tool to probe consciousness at cellular resolution within the intact network. We perform brainwide chemogenetic capture[3,4] of isoflurane anesthesia-activated circuitry in mice —in parallel with electrocorticography[5], wireless mechano-acoustic recording of peripheral physiology[6], and behavioral classification[7,8]— to describe a synthetic state of altered consciousness generated in the absence of an anesthetic agent. We define patterns of activation under isoflurane using intact brain immediate early gene mapping[9–12] combined with brainwide high density silicon probe recordings[13]. Our data identify subcortical hotspots of neural activity in an unconsciousness network that is globally characterized by increased functional connectivity driven by select nodes. We provide technical resources spanning brainwide single-cell resolution maps and neurophysiologic datasets of the isoflurane-rendered unconscious state, along with an approach to further probe its global cellular-level mechanisms.

Together, we present the foundation for future research to refine this viral-genetic brainwide approach to generate synthetic conscious state transitions, such as sleep, stasis, analgesia or anesthesia.

Main Text:

A cell-targeted, global network approach to manipulating consciousness

Many spatially segregated neural circuits are shown to regulate consciousness or recapitulate distinct components of an unconscious state[1]. The dissection of these individual cell-types and circuits has yielded valuable insights into the regulation of sleep[14–17], arousal[18–24], and anesthesia[25–29] with limited translatability for precise conscious state transitions that could replace current pharmacologic approaches. A single, isolated neural correlate of consciousness has not been identified[2]. We directly test the hypothesis that consciousness is subserved by distinct, globally distributed cells in targetable circuits[30,31]. If this is true, a distributed neural correlate of consciousness exists that can be synthetically targeted to generate precise state transitions.

We harness a preclinical platform to test this theory using the genetic capture of brainwide activity during the anesthesia-induced unconscious state in mice. We then evaluate if synthetic re-activation of those defined global neural substrates could recapitulate or modulate consciousness. We go on to evaluate the intact brainwide pattern of activity in the synthetic state as compared to isoflurane-induced unconsciousness using cellular resolution Fos immediate early gene immunolabeling and light sheet microscopy. Functional network analysis of the brainwide patterns of co-activation or co-suppression indicates 9 key communities form the unconsciousness network. We then extend the Fos-based analysis of activity to temporal single unit neural signatures using brainwide Neuropixels probe recordings. Together, we provide a synthetic platform for

manipulating and analyzing cell-specific activity within the global network along with technical resources that provide key neural substrates for future studies.

Activity-dependent capture of a synthetic unconscious state

If unconsciousness is regulated by discrete brainwide-activated cells rather than a non-specific disruption of neural activity, unconsciousness should be recapitulated by those activated cells. To capture brainwide anesthesia-activated unconsciousness circuitry, Fos-TRAP2 ($Fos^{2A\text{-}iCreER}$)[4] mice received retroorbital injections of AAV-PHP.eB virus expressing Cre-dependent designer receptors engineered to be activated by designer drugs (DREADDs)[3]. 3-4 weeks later, mice underwent 180-min of isoflurane exposure (1.2-1.3%) and halfway through the exposure, at 90-min, received an injection of 4-hydroxytamoxifen (4-OHT) to induce activity-dependent DREADD expression in brainwide isoflurane-activated cells (TRAP)[4,32]. On separate subsequent days, mice were implanted with either a wireless mechano-acoustic device[6] or electrodes for electrocorticography to characterize peripheral physiologic and neurophysiologic effects, respectively, as well as behavioral changes after chemogenetic manipulation (Fig 1a).

We first assayed if coordinated movement, as measured in the rotarod test, is affected by chemogenetic stimulation of brainwide anesthesia-activated circuitry. Mice underwent 3 days of training and then were placed on a slowly rotating rod (4 revolutions per minute, rpm) that poses minimal challenge to motor coordination under control conditions. After clozapine-n-oxide (CNO) injection (5 mg/kg), mice expressing activating Gq-DREADD fall off the rotarod when compared to their respective saline trials, indicating a loss of coordinated movement (Fig 1b), which is not observed in mice expressing brainwide inhibitory Gi-DREADD (Extended Fig 1b).

Anesthesia-induced unconsciousness in rodents is commonly defined by loss of righting reflex (LORR)[33], a postural reflex that allows rodents to regain the upright position. This behavioral definition is not used for other altered states of consciousness like after psychedelic treatment[34,35], and there are efforts to identify alternatives to righting reflex for studies of anesthesia-induced unconsciousness[36], such as machine-guided behavioral classification during consciousness state transitions. We find that CNO (10 mg/kg) potentiates LORR with subanesthetic isoflurane administration (Extended Fig 1a). A significant shift toward LORR occurs after synthetic chemogenetic stimulation of isoflurane-activated brainwide circuitry, and not inhibition nor non-TRAP control conditions (Extended Fig 1a). 1 mg/kg and 5 mg/kg CNO produce dose-dependent reduction in movement velocity in activating Gq-DREADD-expressing mice (Extended Fig 1c) but not inhibitory Gi-DREADD-expressing mice (Extended Fig 1d). In behavioral tests, we use 5mg/kg CNO, as that dose is validated to saturate DREADD receptors with minimal off-target effects,[37,38] does not modify behavior when administered to non-TRAP control mice, and does not fully immobilize Gq-DREADD-expressing mice, allowing us to analyze behavioral repertoires of the altered state of consciousness.

Gq-DREADD-expressing mice underwent placement of electrocorticography (ECoG) and electromyography electrodes to assess changes in slow wave delta oscillations in the 1 to 4 Hz frequency range after CNO or saline, as compared to their isoflurane induction (Fig 1c-d, Extended Fig 2). We highlight an approximate “drug onset” dashed line where the average onset of behavioral immobility occurs in CNO trials, typically 10 minutes following injection. Like with isoflurane induction, CNO induction promotes a significant increase in slow wave (1-4 Hz) signal to noise ratio (Fig 1c-d). Group-averaged spectrograms analyzed pre- and post-CNO exposure show a return to baseline occurs 24-hours following the CNO trial (Extended Fig 2b).

We next observed that synthetic stimulation of isoflurane-activated brainwide circuitry produces distinct behaviors, with differing temporal onset and distributions, when mice are tested and recorded in a modified open field chamber in the absence of anesthetic drug. An example raster plot of 6 cumulative saline and CNO trials collected from one Gq-DREADD-expressing mouse shows the representative distribution of 5 behaviors before and after drug onset (Fig 1g, also see Supplemental Video 1). Using machine-guided supervised behavioral classification to quantify behavior relative to control saline injections, we find that induction with CNO results in decreased rearing and grooming behavior, concomitant with an increase in stereotyped circling behavior, Straub tail, and ultimately immobility and freezing (Fig 1h).

Since altered consciousness may be associated with widespread physiologic changes[39], we analyzed peripheral physiologic data collected from wireless mechano-acoustic devices that we previously validated for use under isoflurane[6]. We aligned behavioral and physiological data to the average latency of first loss of immobility observed across CNO induction trials (approximately 10-min after CNO, "drug onset"). Consistent with an altered state of consciousness, we observe significant decreases in body temperature and heart rate recorded after drug onset (Fig 1e-f). Respiratory rate remains unchanged (Extended Fig 1j).

In contrast, we do not observe significant behavioral changes, besides decreased rearing, in brainwide Gi-DREADD-expressing mice (Extended Fig 1e-f). Mice that express Gi-DREADD never show the atypical behaviors, such as Straub tail, seen in the Gq-DREADD mice (Extended Fig 1e-f). They also retain stable peripheral physiology after CNO (Extended Fig 1g-i).

Since anesthesia-induced unconsciousness can encompass analgesia, we sought to identify the anti-nociceptive function of the synthetic state. Mice were tested for thermal anti-nociceptive responses in the warm water tail withdrawal (tail flick) test interleaved with hotplate testing after

saline and at 30-min time points after CNO injection (Fig 1i). In the tail flick test, chemogenetic activation promoted significantly delayed tail withdrawal (Fig 1k). In hotplate testing, chemogenetic activation reduced jumping off the hot plate, decreased paw withdrawals, and increased latency to first response after CNO (Fig 1l). There was no effect of chemogenetic manipulation on thermal anti-nociceptive responding in non-TRAP control or TRAP Gi-DREADD mice at all time points tested (Fig 1k-l). Following all behavioral testing, intact brains were cleared and immunolabeled for DREADD expression using iDisco+ and light sheet microscopy to quantify brainwide DREADD distribution (Fig 1j and Extended Fig 3).

Together, we describe the synthetic induction of an altered state of consciousness that mirrors patterns of behavioral, neural and physiologic activity observed in natural sleep[40], torpor[41,42], and anesthesia[43]. The synthetic state is characterized by a significant increase in 1-4Hz slow wave oscillations, atypical freezing behavior, hypothermia, and loss of coordinated movement. The anti-nociceptive profile accompanying this state transition may be confounded by and reflect the synthetic altered state of consciousness, though it presents a potential platform for dissociating neural circuit components of analgesia and unconsciousness[44], if such a dissociation exists.

Single cell resolution brainwide activity network of isoflurane unconsciousness

To map the neural architecture of synthetically altered consciousness at single cell resolution across the intact brain, we used iDisco+ tissue clearing with mCherry-DREADD immunolabeling followed by light sheet fluorescent microscopy (Extended Fig 3a). Globally, we observe consistent brainwide TRAP2 cell population density across gross cortical and subcortical divisions, besides significant elevations in the hindbrain and decreases in the cerebellum (Extended

Fig 3b). To better understand brain region-specific differences, we used a voxel-based analysis where 3D and 2D TRAP2 density heatmaps exhibit clear patterns of region-specific TRAP2 enrichment (Extended Fig 3c-d, Extended Data Table 3). These expression patterns are not seen in non-TRAP controls (Extended Fig 3e-f).

While the TRAP2 approach is highly specific (>95% of activity labelled cells are Fos+), it is only moderately efficient (~65% of Fos+ cells are activity labeled)[45]. Similarly, following retro-orbital injection at viral titers like our own (2-3x10^{11}), PHP.eB neuron infection efficiency is high in the cortex (~70% of neurons are infected), but moderate in other brain areas like the striatum (~50% of neurons)[46]. Though these transgenic and viral efficiencies are sufficient for inducing robust behavioral changes (Fig 1), they introduce technical bias for analyzing endogenous brainwide structural and functional mechanisms associated with isoflurane-induced unconsciousness.

To overcome this, we apply an unbiased brainwide approach using immunolabeling for the immediate early gene Fos to examine the isoflurane-activated unconsciousness network at cellular resolution. Recent studies using endogenous Fos mapping after isoflurane focused on isolated brain regions such as the hypothalamus using a subanesthetic dose[47] or performed Fos immunolabeling in non-contiguous 2D slices[11] rather than the intact brain. Here, applying an approach that more closely captures globally distributed neurons, we can probe the network-level mechanism of anesthesia-induced altered consciousness in relation to understanding the key cell-specific network nodes engaged in the synthetic altered state.

First, we constructed an intact brainwide functional ‘connectome’ of isoflurane-induced unconsciousness. Mice were anesthetized with isoflurane at 1.2-1.3% for 180-min prior to fixation and intact brain processing (Fig 2a). Control mice were singly housed in the home cage (see

Methods). We used two orthogonal approaches based on different pipelines (ClearMap and UNRAVEL), to analyze our whole brain imaging datasets via cell segmentation, counting, atlas registration, and brain region cell count annotation (Fig 2 and Extended Fig 4-5). We did this to increase analytical rigor through the convergence of key brain regions across analyses. We followed this analysis with network and community analysis in SMARTTR (Fig 3)[12]. Together, these data provide a comprehensive technical resource describing brainwide cellular activation patterns after isoflurane exposure (Fig 2) and an analysis of the brainwide networks to identify key functional communities associated with altered consciousness (Fig 3).

ClearMap and UNRAVEL provide complementary approaches to quantifying Fos density. While ClearMap uses the traditional approach of segmenting cells and performing cell counts within annotated brain regions, UNRAVEL first quantifies bulk signal to identify clusters of significant voxel differences (agnostic to brain atlas region), counts Fos+ cells within these clusters, and summarizes predominant brain regions encompassed by each significant cluster (see Methods for a more detailed discussion). Using both approaches, we find overall differential whole brain activity patterns in the isoflurane state relative to control mice (Fig 2; see Extended Fig 6 for representative images). When analyzed at a gross hierarchical level, the overall total mean Fos density is consistent across analyzed samples, significantly decreases with isoflurane in the isocortex and midbrain, and increases in the olfactory areas, cortical subplate, hypothalamic areas and cerebellum (Extended Fig 4i). At the granular level, isoflurane increases activity within subregions of the striatum (caudoputamen and central amygdala), pallidum (bed nucleus of the stria terminalis), thalamus (paraventricular nucleus), hypothalamus (paraventricular and ventromedial nuclei), and hindbrain (parabrachial nucleus, locus coeruleus, and reticular nucleus) (Fig 2b-d). UNRAVEL confirmed these increases in activity (Fig 2e-h) and extended the findings

(see Supplemental Video 2 and Extended Fig 5). Together, we describe a cortical to subcortical shift in activity in the isoflurane condition with key region-specific subcortical hotspots observed at cellular resolution in the intact brain.

Network analysis reveals high interconnectivity of distributed communities

A given brain state is composed of dynamic interconnectivity between brain regions, so we leveraged our brainwide Fos mapping datasets to investigate how functional activity networks are changed in isoflurane-induced unconsciousness at the cellular resolution (Fig 3). Applying network analysis approaches to study the structure of connectivity (i.e., network topology), can generate insights about the functional patterns that differentiate behavioral states[7–9]. We apply SMARTTR[12], a newly developed accessible R package that supports the importation of externally mapped IEG datasets, for network analysis and visualization. We cross-correlated area-normalized Fos across all mapped subregions (Fig 3a-b) and found a higher number of strongly positive correlations in the isoflurane condition (Extended Fig 7i-j). Since Fos is an activity-dependent marker, positive correlations between brain regions represent either co-activation or co-suppression, while negative correlations represent opposing activation.

To better investigate which individual connections are most functionally altered, we subtracted each regional correlation coefficient in the control condition to its corresponding value in the isoflurane condition and compared each difference to a permuted null distribution. Consistent with our global correlation analysis, there was a greater proportion of positively shifted connections in isoflurane (Fig 3c and Extended Fig 7). We next constructed a functional difference network by visualizing the most significant correlation differences ($p < 0.001$) as connections or edges (lines), and the regions they connect as nodes (circles) (Fig 3d). This network revealed a

naturally high interconnectivity amongst regions with the most functionally different connections, visualized as a large, connected component (i.e., sub-network), rather than as collections of small, isolated networks or individual connections, as would be expected from chance.

Many complex real networks can be broken into subparts called communities, defined by nodes with higher interconnectivity or probability of interconnectivity to other members within their community versus without. We used an agglomerative community detection algorithm[48] and discovered nine distinct communities within our functional difference network (Fig 3d-e). Metrics of nodal influence on a network, termed centrality, include measures such as degree (the number of direct connections to a node) and betweenness (how often a particular node lies on the shortest path between two other nodes). Examination of degree and betweenness (Extended Data Table 8) revealed higher centrality of regions such as the median preoptic nucleus, microcellular tegmental nucleus, lateral mammillary nucleus, locus coeruleus, and lateral parabrachial nucleus. Qualitatively, these metrics align well with the central, influential positioning of these regions within distinct, spatially distributed communities (see Supplemental Video 3).

We also constructed individual networks (edge proportion 3.15%), to examine more general topological properties (Fig 3c and Extended Fig 7). In the context of the brain, the property of small-worldness[49] can be considered a balance between the capacity for functional specialization and integration. We confirmed that both the control and isoflurane networks exhibited small-worldness, defined as $\sigma > 1$, although σ was lower in isoflurane (3.61) compared to control (5.67) (Extended Fig 7d). We examined global network properties across a range of alpha thresholds and proportional thresholds, finding the density of connections in the isoflurane network is consistently higher across a range of alpha thresholds, reflected in the higher trajectories of mean degree, clustering, and efficiency (Extended Fig 7b). This effect is mitigated when

283 controlling for edge density (Extended Fig 7c). As a result, we found that global topological
284 properties are highly influenced by greater functional interconnectivity in the isoflurane
285 unconsciousness network.

286

287 **Heterogeneous brainwide single-unit activity in isoflurane unconsciousness**

288 Since Fos is correlative and only a snapshot of activity, we recorded brainwide single unit
289 activity (Neuropixels) from mice during isoflurane-induced unconsciousness to investigate the
290 natural temporal dynamics of key structures in the network (Fig 4a-b). We summarize neural
291 responses to isoflurane induction and maintenance, comparing them to the mean Fos density
292 difference we observed for each structure between control and isoflurane conditions from our Fos
293 activity map (Fig 4c-d).

294 Consistent with Fos immunolabeling, average population activity was significantly lower
295 in cortical vs subcortical structures following isoflurane exposure (Fig 4c). To examine shared
296 dynamics among distributed neural populations, we performed k-means clustering and identified
297 6 clusters that best described relative activity patterns between induction and maintenance phases
298 (Fig 4d). Clusters were heterogeneous, composed of both cortical and subcortical regions, though
299 in general, clusters with greater relative firing during maintenance contained more subcortical
300 regions compared to those with more cortical subregions. Fos density examined in parallel to each
301 cluster subregion revealed that changes in neural activity generally trended with Fos differences.

302 We highlight neural activity in 3 subregions (reticular nucleus of thalamus, medial
303 amygdalar nucleus and perireunensis nucleus) that showed significantly greater activation by
304 isoflurane in the brainwide Fos analysis (Fig 2, Extended Table 5). A temporal view of the mean
305 normalized firing for these structures during isoflurane induction revealed time-dependent shifts

as well as maintained firing rates throughout induction (Fig 4e). Over the recording session, isoflurane exposure led to broadly reduced firing rates, accounting for relatively low phase averages (Fig 4c-d). Maintenance activity was generally greater than the induction phase mean. When examining recordings across major brain regions, we observed high individual variability within each region, with some units showing greater and others showing lower firing than the average (Extended Fig 8, Extended Tables 9-12). As a result, spatially distributed brain regions demonstrate high heterogeneity in responding to isoflurane-induced unconsciousness, suggesting possible fluctuations of functional interconnectivity occur[50–52].

Discussion

How do we reconcile disparate circuitry and its integration in the global network to shift conscious state? We present a preclinical genetic capture model for dissecting cellular contributions within the intact network. We find that the synthetic state of altered consciousness recapitulates hallmarks of sedation and antinociception, driving slow wave oscillations and increasing subcortical activity while reducing cortical activity. The viral-genetic synthetic model provides a potential neuromodulatory platform for generating precise, desired consciousness state transitions, with applications for inducing sleep, sedation, analgesia or anesthesia when further refined for use outside of a transgenic mouse system. We go on to define the brainwide circuitry captured by the synthetic state compared to isoflurane-induced unconsciousness using intact brain activity mapping and functional network analysis, identifying 9 key communities in the unconsciousness network. Since Fos represents a static, indirect measure of neural activity, we further analyze brainwide neural firing patterns of isoflurane-induced unconsciousness using

Neuropixels high density silicone probes and their comparison to Fos. We find overall increased subcortical activity with heterogeneous responding in any one subregion.

Recent circuit dissection studies in rodents have focused on stimulating or inhibiting isolated brain nuclei to uncover the contributions of individual brain regions to unconsciousness and arousal. These studies provide insights into region-specific contributions in isolation of global brain circuit activity leading to several paradoxical findings. For example, isolated stimulation of the median preoptic nucleus contributes to arousal from anesthesia despite it having high activity during sleep and anesthesia maintenance. Selective stimulation of GABA or glutamate subpopulations in the median preoptic nucleus is insufficient for generating unconsciousness[53]. Our whole brain connectome identifies the median preoptic nucleus as one key community node contributing to the unconscious state. This suggests that the median preoptic nucleus, while significantly regulated by isoflurane, is insufficient to produce unconsciousness in isolation of the brainwide network. Other key community nodes include the lateral parabrachial nucleus and the central amygdala, each found previously to modulate pain responding under anesthesia. Parabrachial nucleus stimulation also does not independently generate unconsciousness, rather accelerates the arousal from an unconscious state[54]. Our findings highlight the complexity of integrating this heterogeneous functional interconnectivity and underline the importance of harnessing an integrated, cell-specific systems-level investigation to understand mechanisms of altered consciousness.

Data availability: Complete datasets are provided in Extended Data Tables. Additional data is available from the corresponding author upon request. Representative videos of behavioral analysis, cluster analysis and community network analysis are provided in Supplemental Videos.

Code availability:

Code for behavioral analysis is available at https://github.com/sgoldenlab/simba .

Code for UNRAVEL analysis is available at https://zenodo.org/records/13655988.

Code for SMARTTR analysis is available at https://mjin1812.github.io/SMARTTR

References:

1. Mashour, G. A. Anesthesia and the neurobiology of consciousness. *Neuron* **112**, 1553–1567 (2024).
2. Koch, C. What Is Consciousness? *Nature* **557**, S8–S12 (2018).
3. Chan, K. Y. *et al.* Engineered AAVs for efficient noninvasive gene delivery to the central and peripheral nervous systems. *Nat Neurosci* **20**, 1172–1179 (2017).
4. DeNardo, L. A. *et al.* Temporal evolution of cortical ensembles promoting remote memory retrieval. *Nat. Neurosci.* **22**, 460–469 (2019).
5. Hsu, Y.-W. A. *et al.* The dorsal medial habenula minimally impacts circadian regulation of locomotor activity and sleep. *J Biol Rhythms* **32**, 444–455 (2017).
6. Ouyang, W. *et al.* An implantable device for wireless monitoring of diverse physio-behavioral characteristics in freely behaving small animals and interacting groups. *Neuron* (2024) doi:10.1016/j.neuron.2024.02.020.
7. Goodwin, N. L. *et al.* Simple Behavioral Analysis (SimBA) as a platform for explainable machine learning in behavioral neuroscience. *Nat Neurosci* **27**, 1411–1424 (2024).
8. Pereira, T. D. *et al.* SLEAP: A deep learning system for multi-animal pose tracking. *Nat Methods* **19**, 486–495 (2022).

9. Renier, N. *et al.* Mapping of Brain Activity by Automated Volume Analysis of Immediate Early Genes. *Cell* **165**, 1789–1802 (2016).

10. Madangopal, R. *et al.* Incubation of palatable food craving is associated with brain-wide neuronal activation in mice. *Proceedings of the National Academy of Sciences* **119**, e2209382119 (2022).

11. Rijsketic, D. R. *et al.* UNRAVELing the synergistic effects of psilocybin and environment on brain-wide immediate early gene expression in mice. *Neuropsychopharmacol.* **48**, 1798–1807 (2023).

12. Jin, M. *et al.* A SMARTR workflow for multi-ensemble atlas mapping and brain-wide network analysis. 2024.07.12.603299 Preprint at https://doi.org/10.1101/2024.07.12.603299 (2024).

13. Jun, J. J. *et al.* Fully integrated silicon probes for high-density recording of neural activity. *Nature* **551**, 232–236 (2017).

14. Ma, C. *et al.* Sleep Regulation by Neurotensinergic Neurons in a Thalamo-Amygdala Circuit. *Neuron* **103**, 323-334.e7 (2019).

15. Ma, C. *et al.* Microglia regulate sleep through calcium-dependent modulation of norepinephrine transmission. *Nat Neurosci* **27**, 249–258 (2024).

16. Zhang, Z. *et al.* An Excitatory Circuit in the Perioculomotor Midbrain for Non-REM Sleep Control. *Cell* **177**, 1293-1307.e16 (2019).

17. Lu, J., Greco, M. A., Shiromani, P. & Saper, C. B. Effect of Lesions of the Ventrolateral Preoptic Nucleus on NREM and REM Sleep. *J. Neurosci.* **20**, 3830–3842 (2000).

18. Silverman, D. *et al.* Activation of locus coeruleus noradrenergic neurons rapidly drives homeostatic sleep pressure. *Sci Adv* **11**, eadq0651 (2025).

19. Taylor, N. E. *et al.* Optogenetic activation of dopamine neurons in the ventral tegmental area induces reanimation from general anesthesia. *Proceedings of the National Academy of Sciences of the United States of America* **113**, 12826–12831 (2016).

20. Castro, D. C. *et al.* An endogenous opioid circuit determines state-dependent reward consumption. *Nature* **598**, 646–651 (2021).

21. Rodriguez-Romaguera, J. *et al.* Prepronociceptin-Expressing Neurons in the Extended Amygdala Encode and Promote Rapid Arousal Responses to Motivationally Salient Stimuli. *Cell Rep* **33**, 108362 (2020).

22. Ramadasan-Nair, R., Hui, J., Itsara, L. S., Morgan, P. G. & Sedensky, M. M. Mitochondrial Function in Astrocytes Is Essential for Normal Emergence from Anesthesia in Mice. *Anesthesiology* **130**, 423–434 (2019).

23. Mashour, G. A., Pal, D. & Brown, E. N. Prefrontal Cortex as a Key Node in Arousal Circuitry. *Trends Neurosci* S0166-2236(22)00144–8 (2022) doi:10.1016/j.tins.2022.07.002.

24. Mashour, G. A. *et al.* Recovery of consciousness and cognition after general anesthesia in humans. *eLife* **10**, e59525 (2021).

25. Brown, E. N., Lydic, R. & Schiff, N. D. General anesthesia, sleep, and coma. *N Engl J Med* **363**, 2638–2650 (2010).

26. Zhang, Z. *et al.* Neuronal ensembles sufficient for recovery sleep and the sedative actions of α2 adrenergic agonists. *Nat Neurosci* **18**, 553–561 (2015).

27. Nelson, L. E. *et al.* The alpha2-adrenoceptor agonist dexmedetomidine converges on an endogenous sleep-promoting pathway to exert its sedative effects. *Anesthesiology* **98**, 428–436 (2003).

28. Zhou, W. *et al.* Activation of orexin system facilitates anesthesia emergence and pain control. *Proceedings of the National Academy of Sciences* **115**, E10740–E10747 (2018).

29. Solovey, G. *et al.* Loss of Consciousness Is Associated with Stabilization of Cortical Activity. *J. Neurosci.* **35**, 10866–10877 (2015).

30. Mashour, G. A., Roelfsema, P., Changeux, J.-P. & Dehaene, S. Conscious Processing and the Global Neuronal Workspace Hypothesis. *Neuron* **105**, 776–798 (2020).

31. Dehaene, S., Kerszberg, M. & Changeux, J.-P. A neuronal model of a global workspace in effortful cognitive tasks. *Proc Natl Acad Sci U S A* **95**, 14529–14534 (1998).

32. DeNardo, L. & Luo, L. Genetic strategies to access activated neurons. *Curr Opin Neurobiol* **45**, 121–129 (2017).

33. Dickinson, R., White, I., Lieb, W. R. & Franks, N. P. Stereoselective Loss of Righting Reflex in Rats by Isoflurane. *Anesthesiology* **93**, 837–843 (2000).

34. Aboharb, F. *et al.* Classification of psychedelics and psychoactive drugs based on brain-wide imaging of cellular c-Fos expression. *Nat Commun* **16**, 1590 (2025).

35. Heifets, B. D. *et al.* Distinct neural mechanisms for the prosocial and rewarding properties of MDMA. *Science Translational Medicine* **11**, eaaw6435 (2019).

36. Gao, S. & Calderon, D. P. Robust alternative to the righting reflex to assess arousal in rodents. *Sci Rep* **10**, 20280 (2020).

37. Manvich, D. F. *et al.* The DREADD agonist clozapine N-oxide (CNO) is reverse-metabolized to clozapine and produces clozapine-like interoceptive stimulus effects in rats and mice. *Sci Rep* **8**, 3840 (2018).

38. Jendryka, M. *et al.* Pharmacokinetic and pharmacodynamic actions of clozapine-N-oxide, clozapine, and compound 21 in DREADD-based chemogenetics in mice. *Sci Rep* **9**, 4522 (2019).

39. Hsueh, B. *et al.* Cardiogenic control of affective behavioural state. *Nature* **615**, 292–299 (2023).

40. Amzica, F. & Steriade, M. Electrophysiological correlates of sleep delta waves. *Electroencephalogr Clin Neurophysiol* **107**, 69–83 (1998).

41. Hrvatin, S. *et al.* Neurons that regulate mouse torpor. *Nature* **583**, 115–121 (2020).

42. Huang, Y.-G. *et al.* The relationship between fasting-induced torpor, sleep, and wakefulness in laboratory mice. *Sleep* **44**, zsab093 (2021).

43. Akeju, O. *et al.* GABAA circuit mechanisms are associated with ether anesthesia-induced unconsciousness. *Clinical Neurophysiology* **127**, 2472–2481 (2016).

44. Weinrich, J. A. *et al.* Paradoxical increases in anterior cingulate cortex activity during nitrous oxide-induced analgesia reveal a signature of pain affect. *bioRxiv* 2023.04.03.534475 (2023) doi:10.1101/2023.04.03.534475.

45. Allen, W. E. *et al.* Thirst-associated preoptic neurons encode an aversive motivational drive. *Science* **357**, 1149–1155 (2017).

46. Chan, K. Y. *et al.* Engineered AAVs for efficient noninvasive gene delivery to the central and peripheral nervous systems. *Nat Neurosci* **20**, 1172–1179 (2017).

47. Wasilczuk, A. Z. *et al.* Hormonal basis of sex differences in anesthetic sensitivity. *Proceedings of the National Academy of Sciences* **121**, e2312913120 (2024).

48. Clauset, A., Newman, M. E. J. & Moore, C. Finding community structure in very large networks. Preprint at https://doi.org/10.48550/arXiv.cond-mat/0408187 (2004).

463 49. Watts, D. J. & Strogatz, S. H. Collective dynamics of 'small-world' networks. *Nature*
464 **393**, 440–442 (1998).
465 50. Huang, Z., Mashour, G. A. & Hudetz, A. G. Propofol disrupts the functional core-matrix
466 architecture of the thalamus in humans. *Nat Commun* **15**, 7496 (2024).
467 51. Vlisides, P. E. *et al.* Dynamic Cortical Connectivity during General Anesthesia in
468 Surgical Patients. *Anesthesiology* **130**, 885–897 (2019).
469 52. Claar, L. D. *et al.* Cortico-thalamo-cortical interactions modulate electrically evoked
470 EEG responses in mice. *eLife* **12**, RP84630 (2023).
471 53. Vanini, G. *et al.* Activation of Preoptic GABAergic or Glutamatergic Neurons Modulates
472 Sleep-Wake Architecture But Not Anesthetic State Transitions. *Current biology : CB* **30**, 779
473 (2020).
474 54. Muindi, F. *et al.* Electrical stimulation of the parabrachial nucleus induces reanimation
475 from isoflurane general anesthesia. *Behav. Brain Res.* **306**, 20–25 (2016).

476

477 **Figure Legends:** *(see combined pdf of all figures with legends)*
478

479 **Figure 1. Synthetic activity-dependent capture of altered consciousness.** (**a**) Experimental
480 timeline: FosTRAP2 transgenic mice received retroorbital injection of an AAV-PHP.eB Cre-
481 dependent Gq-DREADD followed by activity-dependent capture (TRAP) during isoflurane
482 exposure (1.2-1.3%) with 4-hydroxytamoxifen (4-OHT). Mice were tested in the absence of
483 anesthetic after either clozapine-n-oxide (CNO) or saline injection in a modified open field test
484 with concurrent videorecording and peripheral physiology recording using wireless mechano-
485 acoustic (MA) devices, or neural physiology with electrocorticography (ECoG). (DREADD =
486 designer receptor engineered to be activated by a designer drug). (**b**) Gq-DREADD expressing

mice show increased latency to fall off the rotarod at 4-rpm after CNO (n = 7 mice). See Extended Fig 1 for Gi-DREADD data. (**c**) 1-4 Hz delta slow wave activity is prominent after isoflurane induction and (**d**) after CNO injection as compared to saline in Gq-DREADD mice (n = 4, see Extended Fig 2 for spectrograms). (**e**) Left: Heart rate (beats per minute) decreases after CNO injection as compared to saline, shown time-aligned to drug onset, right: mean heart rate decreases after CNO induction in Gq-DREADD mice. (**f**) Left: Body temperature (Celsius) changes over duration of trial, time-aligned to drug onset, right: mean temperature decreases with CNO. (**g**) Representative raster plot from all 6 (3 saline, 3 CNO) of one animal's trials after analysis of classified behavior. (**h**) Bouts of classified behavior for the average of saline and CNO trials per animal (n= 7 mice, total of 18 CNO and 20 saline trials). The average of all saline or CNO trials per animal is shown in b and e-h. Paired t-tests: *p<0.05, **p<0.01. **(i)** Experimental timeline: FosTRAP2 mice received retroorbital injection of either Cre-dependent activating Gq-DREADD or inhibitory Gi-DREADD. They underwent isoflurane exposure, during which either 4-OHT or oil vehicle (if non-TRAP control) was administered. On test day, mice were tested for anti-nociception following saline injection (*Pre*) and after 5 mg/kg CNO. Warm water tail withdrawal (tail flick) latency was tested at 30-, 60-, and 90-minutes (min) post-CNO injection, and hotplate behavior was tested at 30- and 90-min post-CNO injection interleaved with tail flick tests. (**j**) Left: Representative light sheet image after intact brain iDisco+ clearing and mCherry-immunolabeling for DREADD expression, right: mean TRAP Gq-DREADD expression density (n=7 mice). Scale bar is 1 mm and 200 μm in inset. See Extended Fig 3. (**k**) Gq-DREADD mice (n=8, orange) show increased latency to tail flick compared to Gi-DREADD (n=7, blue) or non-TRAP control mice (n=8, gray) at every time point tested. (**l**) In the hot plate test, Gq-DREADD mice do not jump off the hotplate, have fewer paw withdrawals off the hot plate at 90-min, and show increased latency

to first paw withdrawal response at 30 and 90-min post-CNO. 2-way repeated measures ANOVA with Tukey's multiple comparisons: *p<0.05, **p<0.01. Error bars are the mean ± SEM. See Extended Data Tables 1 and 2 for detailed statistics.

Figure 2. Intact whole brain activity mapping of isoflurane unconsciousness at single cell resolution. (a) Experimental overview. Three complementary analytical pipelines were used to analyze whole brain Fos activity map data from the control vs. isoflurane test conditions: ClearMap, b-d; UNRAVEL, e-h; and SMARTTR network analysis (see Fig 3). ClearMap registered brains, detected Fos+ cells, generated cell density heat maps, and used them for voxel-wise analyses. UNRAVEL registered brains and preprocessed immunofluorescence images before warping them to atlas space, z-scoring them, averaging hemispheres together, and running intensity-based voxel-wise analyses. Clusters of significant voxels defined by FDR correction were warped to full-resolution tissue space for validation via cell density measurements. **(b)** Mean Fos+ density shown as a heatmap across the intact brain in all isoflurane samples (n=9). **(c)** Mean Fos+ density heatmap across all control (n=7, top row) and isoflurane samples (n=9, bottom row) virtually sliced in the coronal plane at major anatomical subdivisions ('level 2' – see Methods). **(d)** ClearMap atlas registration followed by pairwise analysis of z-scored Fos density by every anatomical subregion (stop-level') in the control vs isoflurane condition after FDR correction ($q < 0.01$). See Extended Table 4 for all raw and z-scored Fos data. Direction of effect in isoflurane relative to control is shown in the bottom bar with green indicating regions of enhanced Fos in isoflurane. (AON: anterior olfactory nucleus, CPu: caudate-putamen, CeA: central amygdala; BNST: bed nucleus of stria terminalis; PVT: paraventricular thalamus; PVH: paraventricular hypothalamus; VMH: ventromedial hypothalamus; SC: superior colliculus; PBN: parabrachial nucleus; LC: locus coeruleus). Where isoflurane either (**e**) suppressed Fos (Control > Isoflurane)

or (**f**) enhanced Fos (Control < Isoflurane) was mapped via UNRAVEL ($q < 0.05$). **e-f**) Clusters were mirrored in 3D brains (see Supplemental Video 2). Valid clusters for each condition are shown in 3D brains and bar graphs. All data is shown as mean ± SEM, *$p < 0.05$, **$p < 0.01$, ***$p < 0.001$, ****$p < 0.001$ (unpaired two-tailed t-tests). **g-h**) Sunburst plots summarize volumes of regions comprising valid clusters (outer rings represent finer anatomical granularity in the CCFv3 hierarchy). Abbreviations are defined in Extended Table 5 with these exceptions: {'a': 'anterior', 'c': 'central nucleus', 'd': 'dorsal', 'l': 'lateral', 'm': 'motor related or medial', 'mo': 'molecular layer', 'p': 'primary or posterior', 'pl': 'posterolateral', 'po': 'preoptic', 'r': 'rostral', 's': 'secondary or supplemental', 'sg': 'superficial gray layer or granule cell layer', 'v': 'ventral'}. **e-h**) Voxel-wise analysis of Fos+ density and validation of significant clusters using UNRAVEL mapped onto major anatomic regions. See Extended Table 5 for details on each valid cluster and raw cell densities for all clusters across multiple FDR thresholds. See Extended Fig 4-6 for additional analysis and representative images of Fos immunolabeling.

Figure 3. Network analysis reveals hubs that functionally differentiate an isoflurane unconscious state. Regional correlation heatmaps for (**a**) Control and (**b**) Isoflurane condition based on Figure 2 ClearMap atlas-registered mean Fos density data. Groupings of subregions by their larger parent regions are shown as sub-facets. (**c**) A combined network (bottom) showing the overlapping functional connectivity patterns of the individual control (top, red) and isoflurane (middle, blue) functional networks with matching network density (edge proportion = 3.15%) and the combined network below (see Extended Fig 7 for proportional thresholding). (**d**) Functional difference network generated by plotting significant permuted regional correlation differences as edges (lines), and the regions they connect as nodes (circles). The uniquely shaded convex hull

polygons denote regions classified as members of the same community. Key community nodes are abbreviated C1: LM = lateral mamillary nucleus ; C2: MnPO = median preoptic nucleus ; C3: LPB = lateral parabrachial nucleus, C4: LA = lateroanterior hypothalamic nucleus; C5: MiTg = microcellular tegmental nucleus; C6: Bar = Barrington nucleus; C7: VTM = ventral tuberomammillary nucleus ; C8: CeA = central amygdalar nucleus; C9: PrEW = pre-Edinger-Westphal nucleus. (**e**) Anatomical distribution of key community nodes identified in (d) and also shown in Supplemental Video 3. See Extended Fig 7 and Extended Tables 6-8 for all abbreviations and detailed statistics.

Figure 4. Single unit temporal dynamics of isoflurane unconsciousness. (**a**) Experiment schematic. Prior to recording sessions, Neuropixels 1.0 probe shanks were coated in DiI for later histological placement. A 5-min awake baseline period was recorded before isoflurane induction. During induction, foot pinch stimuli were delivered to determine loss-of-reflex (LOR), at which point the concentration was reduced to 1.3% to begin steady-state maintenance phase. (**b**) Left: intact iDisco-cleared brains were imaged with light sheet microscopy and registered to the Allen mouse brain atlas to obtain probe tract placements, right: tract visualizations for all recordings. Shared colors represent tracts from the same mouse. (**c**) Z-scored firing rates for induction and maintenance phases averaged across units from each recorded subregion within isocortex (blue), hippocampus (orange), amygdala (red), thalamus (purple) and hypothalamus (brown). Isoflurane induction and maintenance elicited widespread reductions in average activity across cortical and subcortical regions. Normalized mean Fos density associated with each subregion (from Fig 2) is shown to the right. (**d**) K-means clustering of activity across induction and maintenance phases yielded 6 heterogeneous clusters composed of cortical and subcortical regions, generally differentiated by their relative activity between each isoflurane phase. (**e**) Mean z-scored firing

traces for 3 structures found to have significantly elevated Fos expression: reticular nucleus of thalamus (RT), medial amygdalar nucleus (MEA) and perireunensis nucleus (PR). Traces show 2 min before to 14 min following start of induction (left dashed line: "induction onset") and 2 min before to 10 min following onset of maintenance phase (right dashed line: "LOR/maintenance start"). Shaded error indicates 95% confidence interval. Each animal had 2 recording sessions and one recording was left out due to poor signal quality for a total of 7 recording sessions from 4 mice, yielding N=1048 units (Isocortex, n=37; Hippocampus, n=53; Amygdala, n=16; Thalamus, n=883, Hypothalamus, n=59). D, dorsal; V, ventral; A, anterior; P, posterior. See Extended Fig 8 for representative traces from all major brain regions and Extended Tables 10-11 for data with detailed subpopulation abbreviations.

Extended Figure Legends:

Extended Figure 1. Effects of chemogenetic inhibition after synthetic activity-dependent capture of altered consciousness. (**a**) The concentration of isoflurane (%), as measured with a gas analyzer sampling from the chamber, at which mice display loss of righting reflex during saline or CNO (10 mg/kg) is significantly reduced in Gq-DREADD but not Gi-DREADD or non-TRAP control (n = 5-6 mice). (**b**) There is no change in rotarod (4-rpm) performance in Gi-DREADD mice after 5 mg/kg CNO (n = 5 mice). CNO induces dose-dependent reduction in maximum speed (m/s) in the open field only in (**c**) Gq-DREADD mice (n = 6 mice) and not (**d**) Gi-DREADD mice (n = 5 mice, 3-4 trials per drug condition). (**e**) Representative raster plot from all 6 (3 saline, 3 CNO) of one Gi-DREADD animal's trials after analysis of classified behavior. (**f**) Bouts of classified behavior for the average of saline and CNO (5 mg/kg) trials per animal expressing inhibiting Gi-DREADD virus (n = 5 mice). There is no change in (**g**) heart rate (BPM, beats per

minute) (**h**) respiratory rate (breaths per minute) and (**i**) temperature (Celsius) as recorded from the wireless mechano-acoustic device during trials shown in e-f (n = 6 mice, 2-3 trials per drug condition). (**j**) Respiratory rate in Gq-DREADD TRAP mice is also unchanged. Drug onset time is approximated by average onset of immobility in Gq-DREADD mice (approx. 10 minutes after CNO injection). See Figure 1 and Methods for experimental details. Error bars show mean ± SEM. 2-way repeated measures ANOVA with Tukey's post-hoc tests (panel c-d) and paired *t*-tests, *p<0.05, **p<0.01, ***p<0.001. See Extended Data Table 1 for statistics.

Extended Figure 2. Electrocorticography recordings of the synthetic unconscious state. (**a**) Experimental timeline: FosTRAP2 transgenic mice received retroorbital AAV injection expressing Gq-DREADD and activity-dependent capture during isoflurane exposure, followed by neural electrocorticography (ECoG) recordings over five days (DREADD = designer receptor engineered to be activated by a designer drug, 4-OHT = 4-hydroxytamoxifen, ECoG = electrocorticography, CNO = clozapine n-oxide, ISO = isoflurane). (**b**) Day 1 (labeled "1 - Pre") shows the average 40-minute baseline recording without manipulations. Recordings on Days 2-4 were time-aligned to the approximated onset of intraperitoneal CNO (10 min post-injection) indicated by the white dotted line. Day 5 (labeled "5 - Post") was obtained without drug manipulation. The spectrograms shown are an average of 4 mice. See Fig 1c-d, Extended Data Table 1 and Methods for further details and statistical analysis.

Extended Figure 3. **DREADD immunolabeling after synthetic activity-dependent capture.** (**a**) Experimental timeline: FosTRAP2 transgenic mice received retroorbital injection of an AAV-PHP.eB Cre-dependent Gq-DREADD followed by activity-dependent capture (TRAP) during

627 isoflurane exposure with 4-hydroxytamoxifen (4-OHT). After experiments, intact brains were
628 immunolabeled for mCherry-DREADD and cleared by iDisco+. ClearMap was used to register
629 brains, detect Fos+ cells, and generate cell counts and density heat maps. (**b**) Mean TRAP+ cell
630 density calculated across larger brain subdivisions after atlas registration by ClearMap shows
631 similar TRAP+ cell density across the brain, except for significant differences in the hindbrain and
632 cerebellum (1-way ANOVA, *p<0.05). (**c**) 3-dimensional mean density heatmap (n=7 mice). (**d**)
633 Mean TRAP+ density across all samples shown as voxel-based 2D-projection heatmaps
634 (calibration bar is arbitrary units). (**e**) Representative whole brain light sheet microscopy images
635 after iDisco clearing and mCherry-DREADD immunolabeling digitally sliced to the 2D coronal
636 plane from one control mouse expressing retroorbital AAV-PHP.eB Cre-dependent Gq-DREADD
637 with oil vehicle administered during isoflurane exposure (non-TRAP control, see Methods) and
638 (**f**) one Gq-DREADD-expressing mouse that received 4-OHT during isoflurane exposure for
639 activity-dependent capture of synthetic unconscious state. Abbreviations: SSp= primary
640 somatosensory cortex, HDB = horizontal limb of diagonal band, BMA = basomedial amygdala,
641 VMH = ventromedial hypothalamus, MiTG = microcellular tegmental nucleus, PrCnF =
642 precuneiform area, PNO = pontine reticular, MnR = median raphe nucleus. Scale bar for full
643 coronal slices is 1mm, inset scale bar is 500 µm.
644
645 **Extended Figure 4. Fos activity mapping reveals subcortical isoflurane-activated hotspots.**
646 (**a**) Intact whole brains were imaged horizontally with light sheet microscopy to acquire cellular
647 resolution Fos+ signal then digitally resliced in the coronal plane at the indicated AP positions. (**b**)
648 Representative mean intensity projection of the raw 3.6X Fos+ signal from the isoflurane condition
649 virtually re-sliced to the coronal plane at the indicated AP positions. (**c**) Mean Fos+ density in the

control condition across all samples (n=7) shown as a heatmap. (**d**) Mean Fos+ density in the isoflurane condition across all samples (n=9) shown as a heatmap in the indicated AP coronal plane. (**e**) Pairwise comparison of significant Fos+ regions in control vs isoflurane condition with blue indicating higher Fos+ activity in the isoflurane condition and red indicating higher Fos+ activity in control condition. (**f**) 3D mean Fos+ density heatmaps from the isoflurane condition shown as sections in panel d. (**g**) Voxel-wise significance map of regions significantly regulated in the isoflurane (blue) or control (red) conditions. (**h**) Representative raw Fos+ immunolabeling at the indicated regions: CeL = centrolateral amygdala; BNST = bed nucleus of stria terminalis; PVH = paraventricular hypothalamus; VMH = ventromedial hypothalamus; PBN = parabrachial nucleus; LC = locus coeruleus. (**i**) Mean Fos density calculated across larger brain subdivisions after atlas registration by ClearMap in control vs isoflurane conditions shows significant differences in isocortex, hypothalamus, midbrain and cerebellum. (unpaired t-test, *$p<0.05$). (**j**) Regions significantly activated in isoflurane (blue) or control (red). Scale bars shown are 1mm except in panel h insets where scale bar is 250 µm.

Extended Figure 5. Identification of isoflurane-activated clusters from UNRAVEL analysis. Voxel-wise data from Fig 2e-h were warped to the Allen Mouse Brain Common Coordinate Framework (CCFv3) for display in coronal brain slices, overlaid with a colored wireframe using FSLeyes. Input images for voxel-wise comparisons were averaged for each group to show background-subtracted and z-scored Fos immunofluorescence. FDR-corrected p-value maps show increases (warm colors) and decreases (cool colors) in Fos expression resulting from isoflurane treatment. For each effect direction, the most stringent q-value threshold is fully opaque (100%), the next most stringent is semi-opaque (66%), and the least stringent is less opaque (33%). Valid clusters with significant differences in Fos+ cell density were randomly colored and labeled with

their IDs. Abbreviations: Adj. = adjusted; Avg. = average; SS = somatosensory; OT = olfactory tubercle; SI = substantia innominata; BNST = bed nucleus of the stria terminalis; MA = magnocellular nucleus; PVH = paraventricular hypothalamic nucleus; Hypothal. = hypothalamus; CeA = central amygdala; Thal. = thalamus; ZI = zona incerta; COA = cortical amygdalar area; MB = midbrain; Sup. = superior; PAG = periaqueductal gray; Inf. = inferior.

Extended Figure 6. Representative Fos immunolabeling from cleared intact brains. Images from a representative control **(l**eft column) and an isoflurane mouse (right column) from Figure 2. Images were acquired with a light sheet microscope using a 3.6X objective in the horizontal plane and then re-sliced to the coronal plane to identify (**a**) BNST = bed nucleus of the stria terminalis, (**b**) PVH = paraventricular hypothalamus, (**c**) CeA = central amygdala, (**d**) VMH = ventromedial hypothalamus, (**e**) PBN = parabrachial nucleus, (**f**) LC = locus coeruleus. Scale bars are 1mm for the full coronal slice and 500 um for the inset image.

Extended Figure 7. Isoflurane networks are denser across a variety of weight thresholds. (**a**) control (red) and isoflurane (blue) networks thresholded at various alpha values. (**b**) Mean degree, clustering, betweenness, and efficiency metrics calculated across a range of significance thresholds and (**c**) edge proportion thresholds. (**d**) Assessment of small-world properties of individual networks plotted in Fig 3. Small-world index (σ) for both networks are above the threshold of 1 (black dotted horizontal line). The control network (**e**) clustering coefficient and (**f**) path length as well as the isoflurane (**g**) clustering coefficient and (**h**) path length are higher than randomly rewired networks with matching degree sequences. (**i**) Distributions of the Pearson correlation coefficients between all unique regional connections and their associated (**j**) p-value for the control and isoflurane networks. (**k**) Volcano plot illustrating the regional correlations which most differ

between the networks. The horizontal red line denotes a significance threshold of $p < 0.001$. Red points in the upper right (control < isoflurane) and upper left quadrants (control > isoflurane), defined by vertical red line lines, indicate regional correlation differences with a magnitude shift greater than 1 between groups. Two-tailed Students *t*-test: **p<0.01, ****p<0.0001. Error bars represent mean ± SEM. See Extended Data Tables 6-8 for full abbreviations and detailed statistics.

Extended Figure 8. Response variability during isoflurane. (**a**) Heatmaps showing mean normalized firing for each major region (isocortex, hippocampus, amygdala, thalamus, and hypothalamus) across anesthetic phases (induction, maintenance, washout) with the total unit counts (*n*) for each region. (**b**) Representative traces from units in major regions with diverse responses under isoflurane. For each major region, traces show 5 units (*k*=5 from total unit count *n* for each region) with the highest (top) and lowest (bottom) mean normalized firing during the maintenance phase. Left traces show 1 min prior and 5 min following onset of induction at the dashed line ("ISO on"). Right traces show 1 min prior and 10 min following onset of maintenance phase (first dashed line) and the "ISO off" time (right dashed line). (**c**) Mean z-scored firing from each experimental phase was clustered (Ward's method) for all subregions obtained in recordings. Hierarchical clustering of subpopulation means revealed 3 heterogeneous clusters (CHI=11.12), each with subclusters (e.g., 1a: Cluster 1a) linking spatially distributed cortical and subcortical structures. See Extended Table 9 and Extended Table 12 for detailed data.

719 **Supplemental Videos (3):**

720 **Supplemental Video 1. Behavioral video analysis of synthetic activity-dependent capture of**
721 **unconsciousness.** Representative video clips at 4X speed from one Gq-DREADD TRAP mouse's
722 saline and CNO trials (see Fig 1c).

723

724 **Supplemental Video 2. UNRAVEL identification of isoflurane-activated clusters video.**
725 Rotating 3D brain models depict valid clusters representing differences in Fos expression and Fos+
726 cell density in response to isoflurane treatment (see Fig 2e-h**).** The direction of change relative to
727 the control condition is indicated. Valid cluster maps were mirrored to display a bilateral
728 representation for visualization purposes.

729

730 **Supplemental Video 3. Anatomical distribution of community network analysis video.**
731 Rotating 3D brains depict key community nodes from functional network analysis (see Fig 3).

732

733 **Extended Data Tables (12):**

734 ST1: Detailed statistics for Figure 1 and Extended Figure 1

735 ST2: Feature importance and model metrics

736 ST3: TRAP analysis - TRAP ClearMap counts table for EF3

737 ST4: Fos whole brain raw data, z scores and ClearMap significant region stats

738 ST5: UNRAVEL whole brain statistics

739 ST6: Permutation results, control vs. isoflurane

740 ST7: Unique regions analyzed: abbreviations from network analysis

741 ST8: Permutation network node centrality- community results

742 ST9: Maximal and minimal brain wide firing

743 ST10: Subregion firing means

744 ST11: K-means clustering firing means

745 ST12: Hierarchical clustering firing means

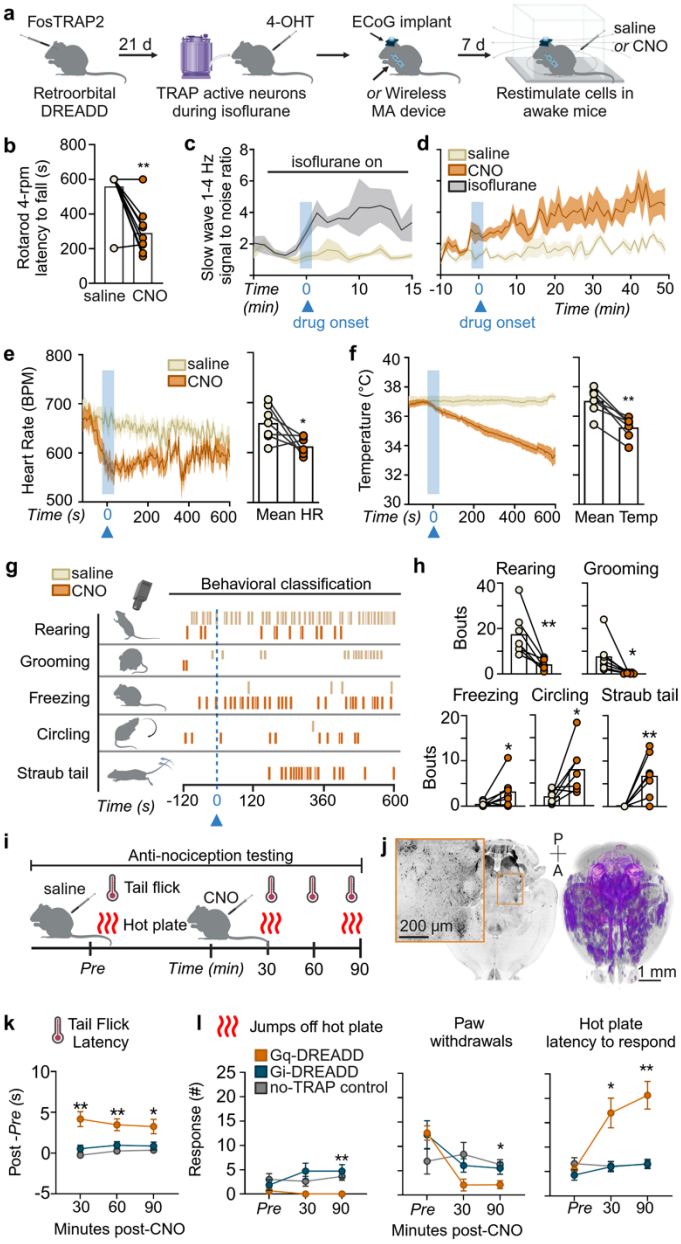

Figure 1. Synthetic activity-dependent capture of altered consciousness. (**a**) Experimental timeline: FosTRAP2 transgenic mice received retroorbital injection of an AAV-PHP.eB Cre-dependent Gq-DREADD followed by activity-dependent capture (TRAP) during isoflurane exposure (1.2-1.3%) with 4-hydroxytamoxifen (4-OHT). Mice were tested in the absence of anesthetic after either clozapine-n-oxide (CNO) or saline injection in a modified open field test with concurrent videorecording and peripheral physiology recording using wireless mechano-acoustic (MA) devices, or neural physiology with electrocorticography (ECoG). (DREADD = designer receptor engineered to be activated by a designer drug). (**b**) Gq-DREADD expressing mice show increased latency to fall off the rotarod at 4-rpm after CNO (n = 7 mice). See Extended Fig 1 for Gi-DREADD data. (**c**) 1-4 Hz delta slow wave activity is prominent after isoflurane induction and (**d**) after CNO injection as compared to saline in Gq-DREADD mice (n = 4, see Extended Fig 2 for spectrograms). (**e**) Left: Heart rate (beats per minute) decreases after CNO injection as compared to saline, shown time-aligned to drug onset, right: mean heart rate decreases after CNO induction in Gq-DREADD mice. (**f**) Left: Body temperature (Celsius) changes over duration of trial, time-aligned to drug onset, right: mean temperature decreases with CNO. (**g**) Representative raster plot from all 6 (3 saline, 3 CNO) of one animal's trials after analysis of classified behavior. (**h**) Bouts of classified behavior for the average of saline and CNO trials per animal (n= 7 mice, total of 18 CNO and 20 saline trials). The average of all saline or CNO trials per animal is shown in b and e-h. Paired t-tests: *p<0.05, **p<0.01. **(i)** Experimental timeline: FosTRAP2 mice received retroorbital injection of either Cre-dependent activating Gq-DREADD or inhibitory Gi-DREADD. They underwent isoflurane exposure, during which either 4-OHT or oil vehicle (if non-TRAP control) was administered. On test day, mice were tested for anti-nociception following saline injection (*Pre*) and after 5 mg/kg CNO. Warm water tail withdrawal (tail flick) latency was tested at 30-, 60-, and 90-minutes (min) post-CNO injection, and hotplate behavior was tested at 30- and 90-min post-CNO injection interleaved with tail flick tests. (**j**) Left: Representative light sheet image after intact brain iDisco+ clearing and mCherry-immunolabeling for DREADD expression, right: mean TRAP Gq-DREADD expression density (n=7 mice). Scale bar is 1 mm and 200 µm in inset. See Extended Fig 3. (**k**) Gq-DREADD mice (n=8, orange) show increased latency to tail flick compared to Gi-DREADD (n=7, blue) or non-TRAP control mice (n=8, gray) at every time point tested. (**l**) In the hot plate test, Gq-DREADD mice do not

jump off the hotplate, have fewer paw withdrawals off the hot plate at 90-min, and show increased latency to first paw withdrawal response at 30 and 90-min post-CNO. 2-way repeated measures ANOVA with Tukey's multiple comparisons: *p<0.05, **p<0.01. Error bars are the mean ± SEM. See Extended Data Tables 1 and 2 for detailed statistics.

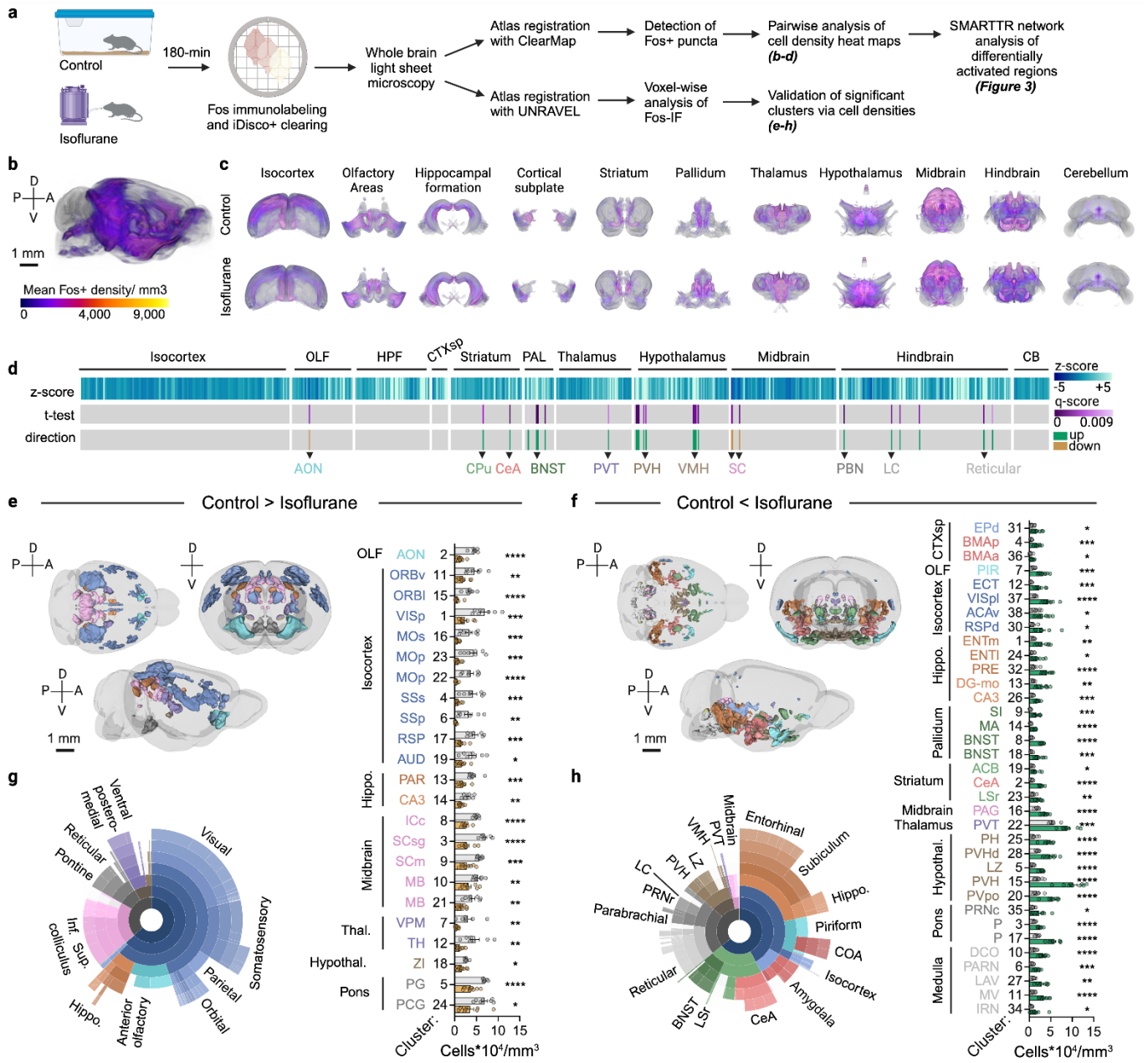

Figure 2. Intact whole brain activity mapping of isoflurane unconsciousness at single cell resolution. (a) Experimental overview. Three complementary analytical pipelines were used to analyze whole brain Fos activity map data from the control vs. isoflurane test conditions: ClearMap, b-d; UNRAVEL, e-h; and SMARTTR network analysis, see Fig 3). ClearMap registered brains, detected Fos+ cells, generated cell density heat maps, and used them for voxel-wise analyses. UNRAVEL registered brains and preprocessed immunofluorescence images before warping them to atlas space, z-scoring them, averaging hemispheres together, and running intensity-based voxel-wise analyses. Clusters of significant voxels defined by FDR correction were warped to full-resolution tissue space for validation via cell density measurements. (**b)** Mean Fos+ density shown as a heatmap across the intact brain in all isoflurane samples (n=9). (**c)** Mean Fos+ density heatmap across all control (n=7, top row) and isoflurane samples (n=9, bottom row) virtually sliced in the coronal plane at major anatomical subdivisions ('level 2' – see Methods). (**d)** ClearMap atlas registration followed by pairwise analysis of z-scored Fos density by every anatomical subregion (stop-level') in the control vs isoflurane condition after FDR correction ($q < 0.01$). See Extended Table 4 for all raw and z-scored Fos data. Direction of effect in isoflurane relative to control is shown in the bottom bar with green indicating regions of enhanced Fos in isoflurane. (AON: anterior olfactory nucleus, CPu: caudate-putamen, CeA: central amygdala; BNST: bed nucleus of stria terminalis; PVT: paraventricular thalamus; PVH: paraventricular hypothalamus; VMH: ventromedial hypothalamus; SC: superior colliculus; PBN: parabrachial nucleus; LC: locus coeruleus). Where isoflurane either (**e**) suppressed Fos (Control > Isoflurane) or (**f**) enhanced Fos (Control < Isoflurane) was mapped via UNRAVEL ($q < 0.05$). **e-f**) Clusters were mirrored in 3D brains (see Supplemental Video 2). Valid clusters for each condition are shown in 3D brains and bar graphs. All data is shown as mean ± SEM, *$p < 0.05$, **$p < 0.01$, ***$p < 0.001$, ****$p < 0.001$ (unpaired two-tailed t-tests). **g-h**) Sunburst plots summarize volumes of regions comprising valid clusters (outer rings represent finer anatomical granularity in the CCFv3 hierarchy). Abbreviations are defined in Extended Table 5 with these exceptions: {'a': 'anterior', 'c': 'central nucleus', 'd': 'dorsal', 'l': 'lateral', 'm': 'motor related or medial', 'mo': 'molecular layer', 'p': 'primary or posterior', 'pl': 'posterolateral', 'po': 'preoptic', 'r': 'rostral', 's': 'secondary or supplemental', 'sg': 'superficial gray layer or granule cell layer', 'v': 'ventral'}. **e-h**) Voxel-wise analysis of Fos+ density and validation of significant clusters using UNRAVEL

mapped onto major anatomic regions. See Extended Table 5 for details on each valid cluster and raw cell densities for all clusters across multiple FDR thresholds. See Extended Fig 4-6 for additional analysis and representative images of Fos immunolabeling.

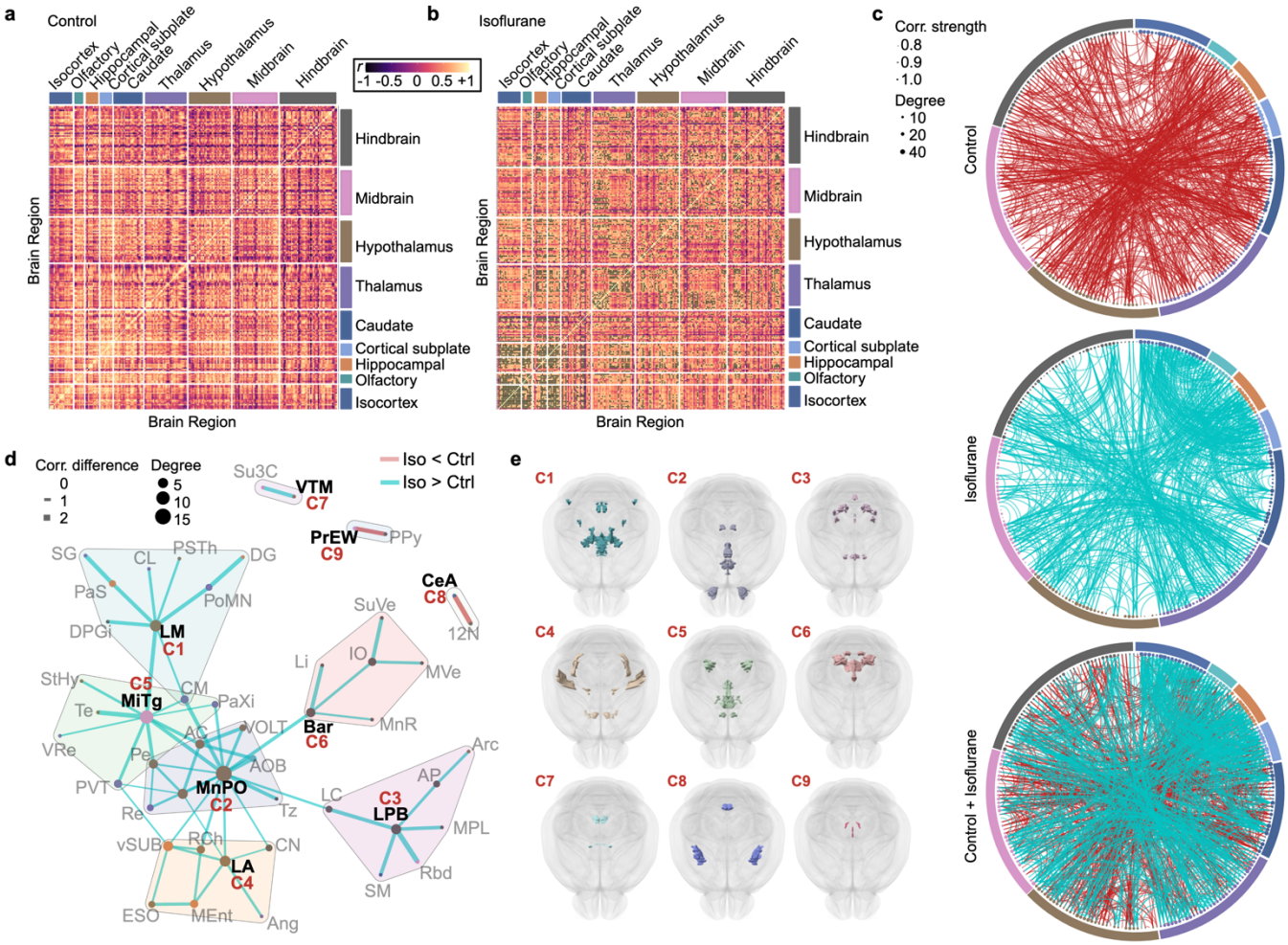

Figure 3. Network analysis reveals hubs that functionally differentiate an isoflurane unconscious state. Regional correlation heatmaps for (**a**) Control and (**b**) Isoflurane condition based on Figure 2 ClearMap atlas-registered mean Fos density data. Groupings of subregions by their larger parent regions are shown as sub-facets. (**c)** A combined network (bottom) showing the overlapping functional connectivity patterns of the individual control (top, red) and isoflurane (middle, blue) functional networks with matching network density (edge proportion = 3.15%) and the combined network below (see Extended Fig 7 for proportional thresholding). (**d**) Functional difference network generated by plotting significant permuted regional correlation differences as edges (lines), and the regions they connect as nodes (circles). The uniquely shaded convex hull polygons denote regions classified as members of the same community. Key community nodes are abbreviated C1: LM = lateral mamillary nucleus ; C2: MnPO = median preoptic nucleus ; C3: LPB = lateral parabrachial nucleus, C4: LA = lateroanterior hypothalamic nucleus; C5: MiTg = microcellular tegmental nucleus; C6: Bar = Barrington nucleus; C7: VTM = ventral tuberomammillary nucleus ; C8: CeA = central amygdalar nucleus; C9: PrEW = pre-Edinger-Westphal nucleus. (**e**) Anatomical distribution of key community nodes identified in (d) and also shown in Supplemental Video 3. See Extended Fig 7 and Extended Tables 6-8 for all abbreviations and detailed statistics.

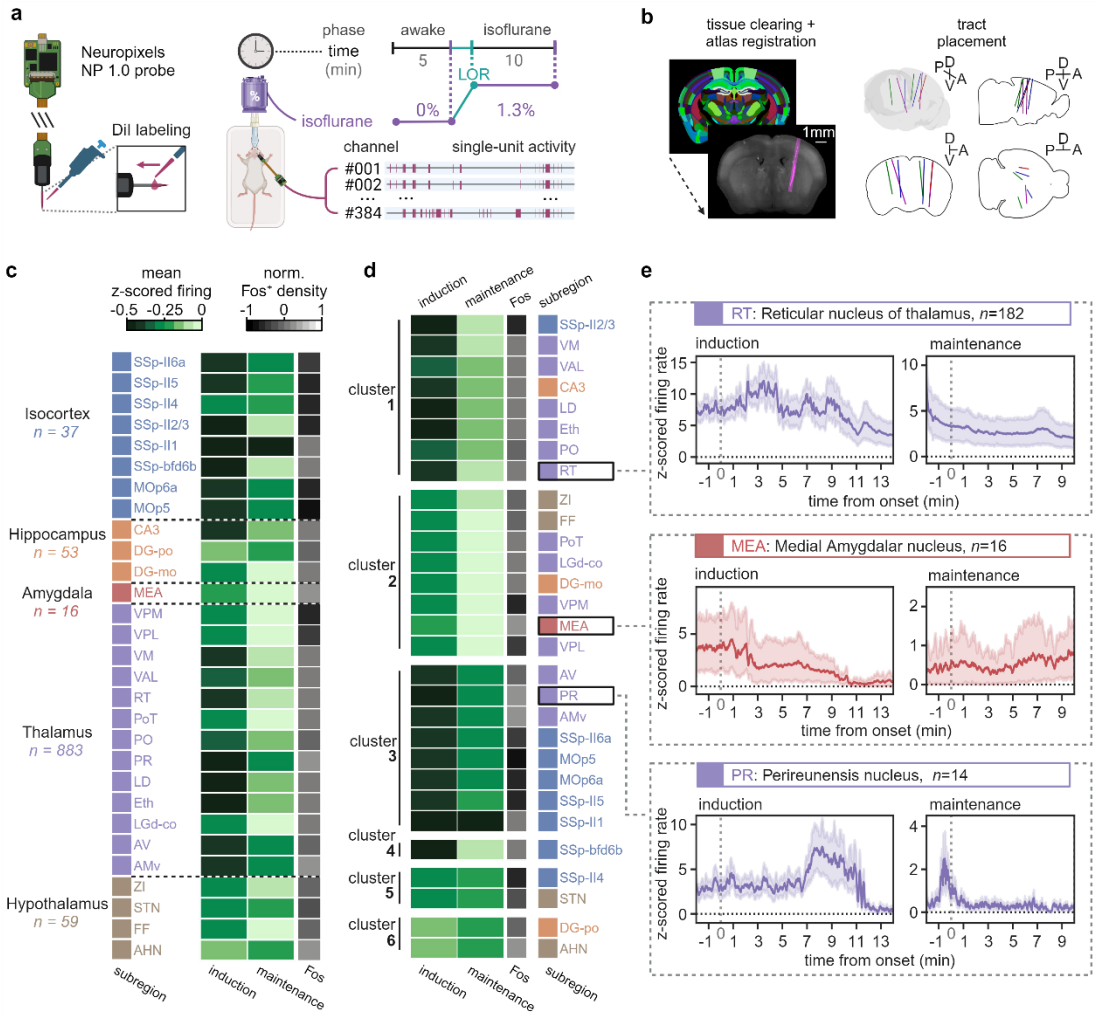

Figure 4. Single unit temporal dynamics of isoflurane unconsciousness. (**a**) Experiment schematic. Prior to recording sessions, Neuropixels 1.0 probe shanks were coated in DiI for later histological placement. A 5-min awake baseline period was recorded before isoflurane induction. During induction, foot pinch stimuli were delivered to determine loss-of-reflex (LOR), at which point the concentration was reduced to 1.3% to begin steady-state maintenance phase. (**b**) Left: intact iDisco-cleared brains were imaged with light sheet microscopy and registered to the Allen mouse brain atlas to obtain probe tract placements, right: tract visualizations for all recordings. Shared colors represent tracts from the same mouse. (**c**) Z-scored firing rates for induction and maintenance phases averaged across units from each recorded subregion within isocortex (blue), hippocampus (orange), amygdala (red), thalamus (purple) and hypothalamus (brown). Isoflurane induction and maintenance elicited widespread reductions in average activity across cortical and subcortical regions. Normalized mean Fos density associated with each subregion (from Fig 2) is shown to the right. (**d**) K-means clustering of activity across induction and maintenance phases yielded 6 heterogeneous clusters composed of cortical and subcortical regions, generally differentiated by their relative activity between each isoflurane phase. (**e**) Mean z-scored firing traces for 3 structures found to have significantly elevated Fos expression: reticular nucleus of thalamus (RT), medial amygdalar nucleus (MEA) and perireunensis nucleus (PR). Traces show 2 min before to 14 min following start of induction (left dashed line: “induction onset”) and 2 min before to 10 min following onset of maintenance phase (right dashed line: “LOR/maintenance start”). Shaded error indicates 95% confidence interval. Each animal had 2 recording sessions and one recording was left out due to poor signal quality for a total of 7 recording sessions from 4 mice, yielding N=1048 units (Isocortex, n=37; Hippocampus, n=53; Amygdala, n=16; Thalamus, n=883, Hypothalamus, n=59). D, dorsal; V, ventral; A, anterior; P, posterior. See Extended Fig 8 for representative traces from all major brain regions and Extended Tables 10-11 for data with detailed subpopulation abbreviations.

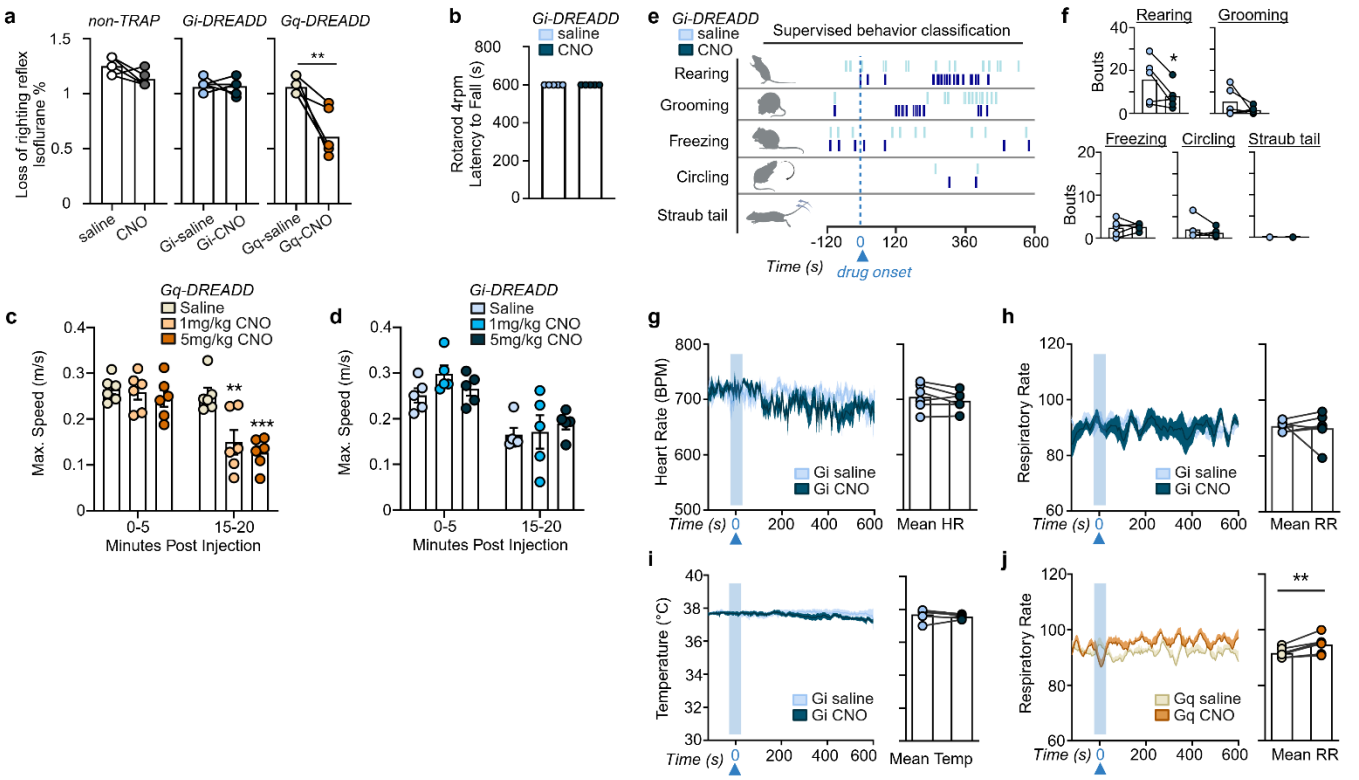

Extended Figure 1. Effects of chemogenetic inhibition after synthetic activity-dependent capture of altered consciousness. (**a**) The concentration of isoflurane (%), as measured with a gas analyzer sampling from the chamber, at which mice display loss of righting reflex during saline or CNO (10 mg/kg) is significantly reduced in Gq-DREADD but not Gi-DREADD or non-TRAP control (n = 5-6 mice). (**b**) There is no change in rotarod (4-rpm) performance in Gi-DREADD mice after 5 mg/kg CNO (n = 5 mice). CNO induces dose-dependent reduction in maximum speed (m/s) in the open field only in (**c**) Gq-DREADD mice (n = 6 mice) and not (**d**) Gi-DREADD mice (n = 5 mice, 3-4 trials per drug condition). (**e**) Representative raster plot from all 6 (3 saline, 3 CNO) of one Gi-DREADD animal's trials after analysis of classified behavior. (**f**) Bouts of classified behavior for the average of saline and CNO (5 mg/kg) trials per animal expressing inhibiting Gi-DREADD virus (n = 5 mice). There is no change in (**g**) heart rate (BPM, beats per minute) (**h**) respiratory rate (breaths per minute) and (**i**) temperature (Celsius) as recorded from the wireless mechano-acoustic device during trials shown in e-f (n = 6 mice, 2-3 trials per drug condition). (**j**) Respiratory rate in Gq-DREADD TRAP mice is also unchanged. Drug onset time is approximated by average onset of immobility in Gq-DREADD mice (approx. 10 minutes after CNO injection). See Figure 1 and Methods for experimental details. Error bars show mean ± SEM. 2-way repeated measures ANOVA with Tukey's post-hoc tests (panel c-d) and paired *t*-tests, *p<0.05, **p<0.01, ***p<0.001. See Extended Data Table 1 for statistics.

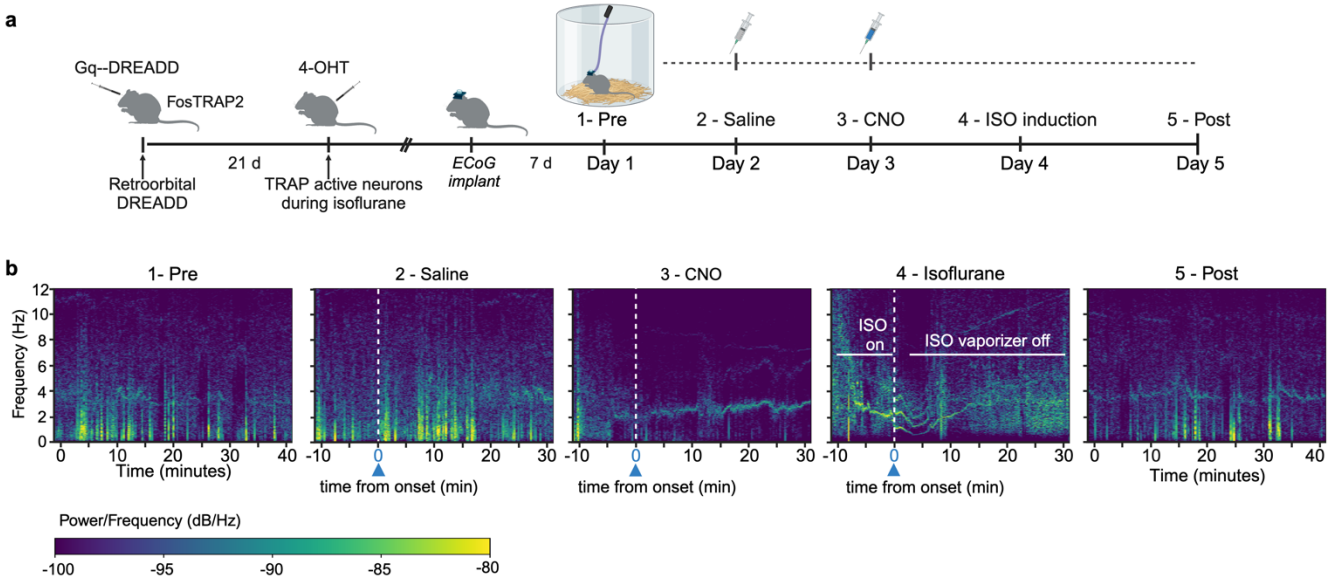

Extended Figure 2. Electrocorticography recordings of the synthetic unconscious state. (**a**) Experimental timeline: FosTRAP2 transgenic mice received retroorbital AAV injection expressing Gq-DREADD and activity-dependent capture during isoflurane exposure, followed by neural electrocorticography (ECoG) recordings over five days (DREADD = designer receptor engineered to be activated by a designer drug, 4-OHT = 4-hydroxytamoxifen, ECoG = electrocorticography, CNO = clozapine n-oxide, ISO = isoflurane). (**b**) Day 1 (labeled “1 - Pre”) shows the average 40-minute baseline recording without manipulations. Recordings on Days 2-4 were time-aligned to the approximated onset of intraperitoneal CNO (10 min post-injection) indicated by the white dotted line. Day 5 (labeled “5 - Post”) was obtained without drug manipulation. The spectrograms shown are an average of 4 mice. See Figure 1c-d, Extended Data Table 1 and Methods for further statistical analysis.

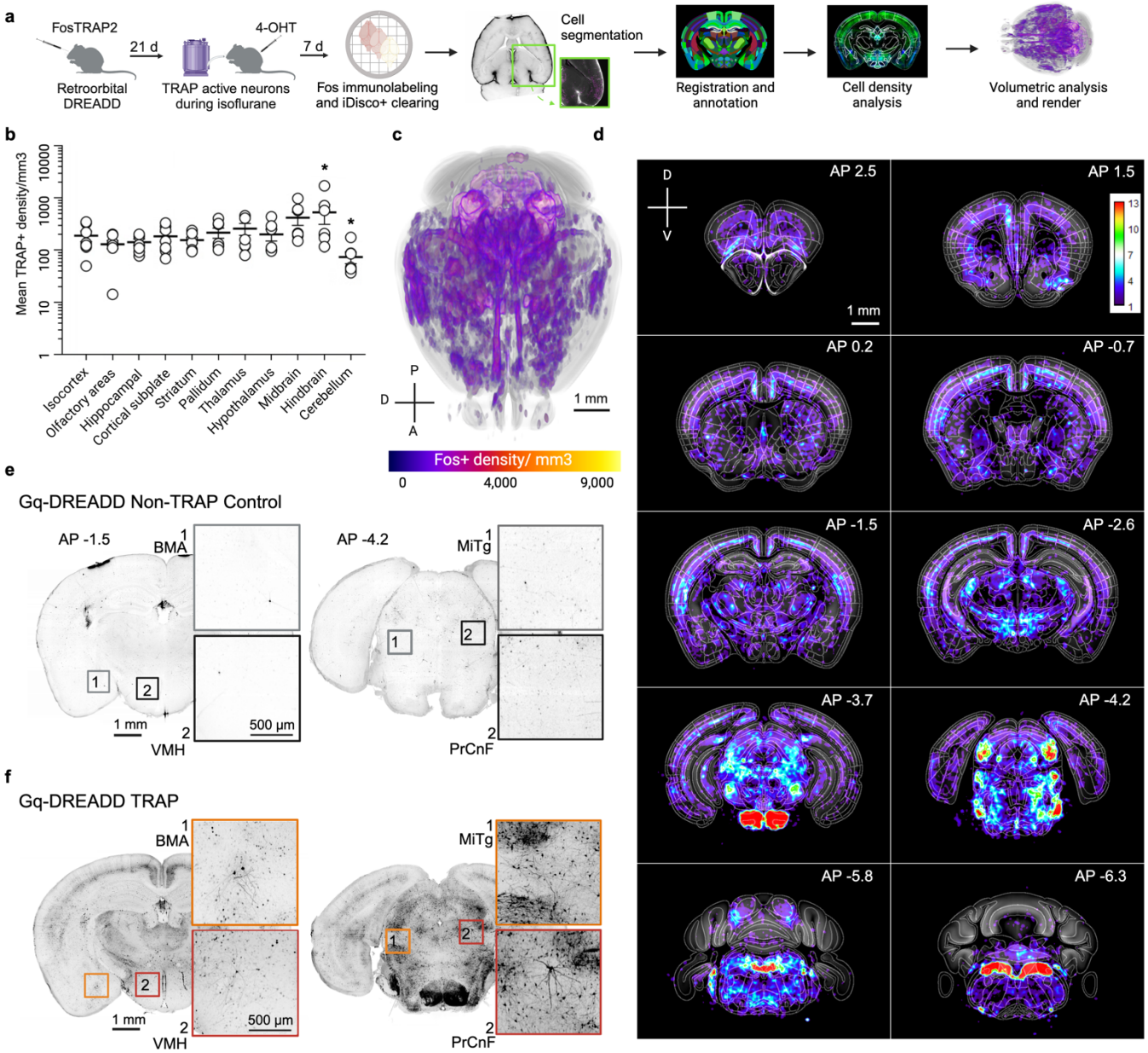

Extended Figure 3. **DREADD immunolabeling after synthetic activity-dependent capture.** (**a**) Experimental timeline: FosTRAP2 transgenic mice received retroorbital injection of an AAV-PHP.eB Cre-dependent Gq-DREADD followed by activity-dependent capture (TRAP) during isoflurane exposure with 4-hydroxytamoxifen (4-OHT). After experiments, intact brains were immunolabeled for mCherry-DREADD and cleared by iDisco+. ClearMap was used to register brains, detect Fos+ cells, and generate cell counts and density heat maps. (**b**) Mean TRAP+ cell density calculated across larger brain subdivisions after atlas registration by ClearMap shows similar TRAP+ cell density across the brain, except for significant differences in the hindbrain and cerebellum (1-way ANOVA, *p<0.05). (**c**) 3-dimensional mean density heatmap (n=7 mice). (**d**) Mean TRAP+ density across all samples shown as voxel-based 2D-projection heatmaps (calibration bar is arbitrary units). (**e**) Representative whole brain light sheet microscopy images after iDisco clearing and mCherry-DREADD immunolabeling digitally sliced to the 2D coronal plane from one control mouse expressing retroorbital AAV-PHP.eB Cre-dependent Gq-DREADD with oil vehicle administered during isoflurane exposure (non-TRAP control, see Methods) and (**f**) one Gq-DREADD-expressing mouse that received 4-OHT during isoflurane exposure for activity-dependent capture of synthetic unconscious state. Abbreviations: SSp= primary somatosensory cortex, HDB = horizontal limb of diagonal band, BMA = basomedial amygdala, VMH = ventromedial hypothalamus, MiTG = microcellular tegmental nucleus, PrCnF = precuneiform area, PNO = pontine reticular, MnR = median raphe nucleus. Scale bar for full coronal slices is 1mm, inset scale bar is 500 µm.

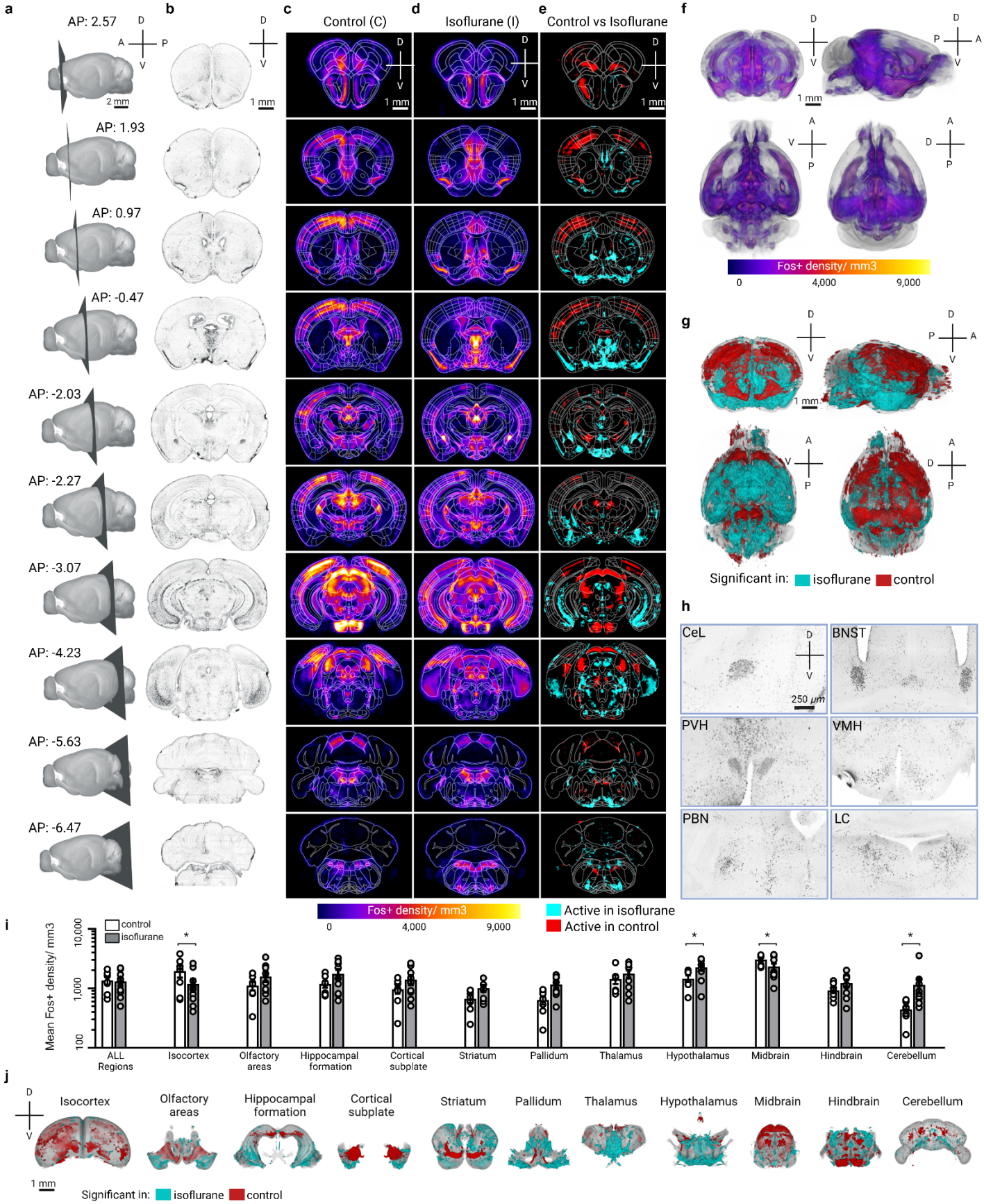

Extended Figure 4. Fos activity mapping reveals subcortical isoflurane-activated hotspots. (**a**) Intact whole brains were imaged horizontally with light sheet microscopy to acquire cellular resolution Fos+ signal then digitally resliced in the coronal plane at the indicated AP positions. (**b**) Representative mean intensity projection of the raw 3.6X Fos+ signal from the isoflurane condition virtually re-sliced to the coronal plane at the indicated AP positions. (**c**) Mean Fos+ density in the control condition across all samples (n=7) shown as a heatmap. (**d**) Mean Fos+ density in the isoflurane condition across all samples (n=9) shown as a heatmap in the indicated AP coronal

plane. (**e**) Pairwise comparison of significant Fos+ regions in control vs isoflurane condition with blue indicating higher Fos+ activity in the isoflurane condition and red indicating higher Fos+ activity in control condition. (**f**) 3D mean Fos+ density heatmaps from the isoflurane condition shown as sections in panel d. (**g**) Voxel-wise significance map of regions significantly regulated in the isoflurane (blue) or control (red) conditions. (**h**) Representative raw Fos+ immunolabeling at the indicated regions: CeL = centrolateral amygdala; BNST = bed nucleus of stria terminalis; PVH = paraventricular hypothalamus; VMH = ventromedial hypothalamus; PBN = parabrachial nucleus; LC = locus coeruleus. (**i**) Mean Fos density calculated across larger brain subdivisions after atlas registration by ClearMap in control vs isoflurane conditions shows significant differences in isocortex, hypothalamus, midbrain and cerebellum. (unpaired t-test, *$p<0.05$). (**j**) Regions significantly activated in isoflurane (blue) or control (red). Scale bars shown are 1mm except in panel h insets where scale bar is 250 μm.

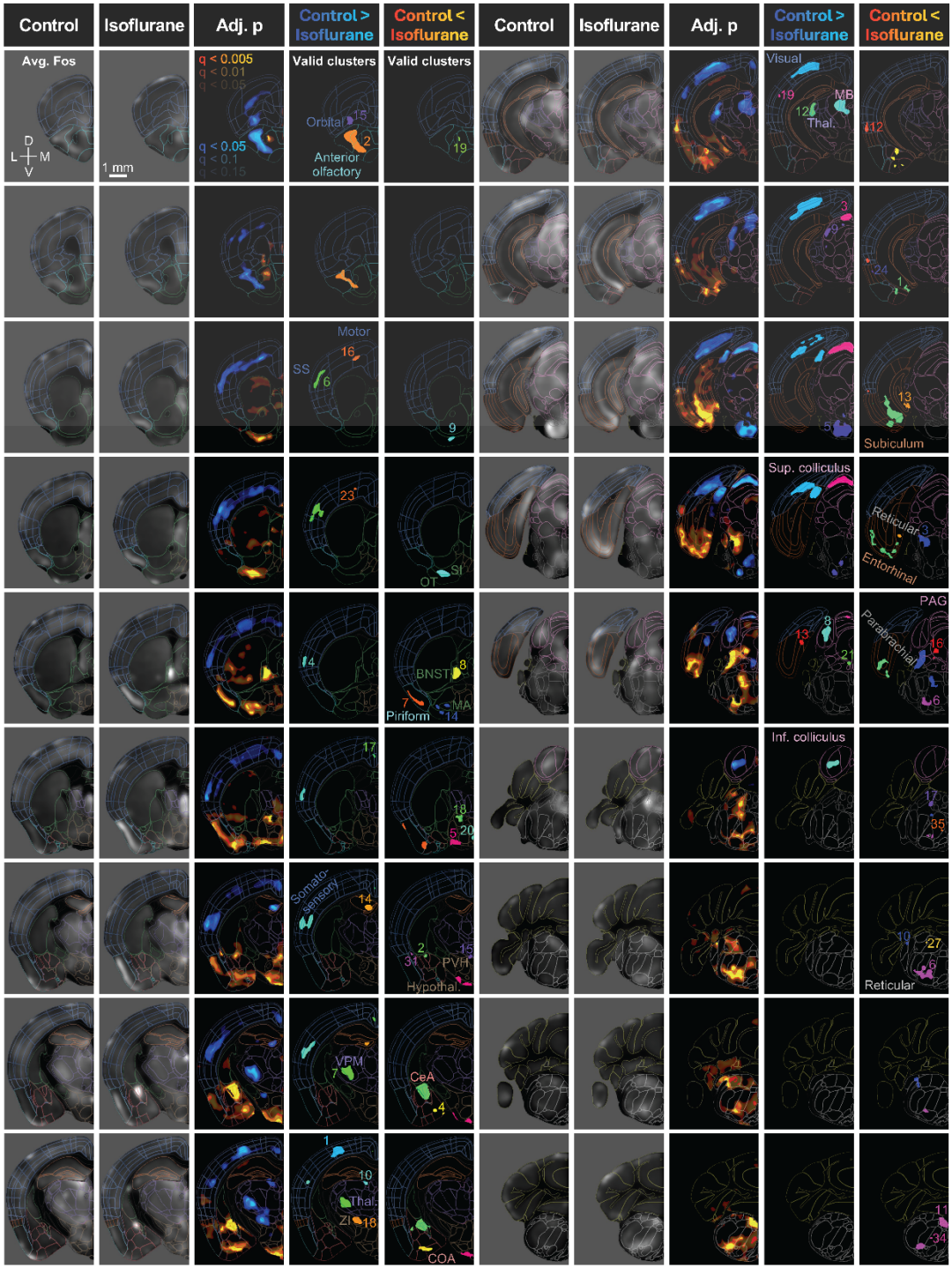

Extended Figure 5. Identification of isoflurane-activated clusters from UNRAVEL analysis. Voxel-wise data from Fig 2e-h were warped to the Allen Mouse Brain Common Coordinate Framework (CCFv3) for display in coronal brain slices, overlaid with a colored wireframe using FSLeyes. Input images for voxel-wise comparisons were averaged for each group to show background-subtracted and z-scored Fos immunofluorescence. FDR-corrected p-value maps show increases (warm colors) and decreases (cool colors) in Fos expression resulting from isoflurane treatment. For each effect direction, the most stringent q-value threshold is fully opaque (100%), the next most stringent is semi-opaque (66%), and the least stringent is less opaque (33%). Valid clusters with significant differences in Fos+ cell density were randomly colored and labeled with their IDs. Abbreviations: Adj. = adjusted; Avg. = average; SS = somatosensory; OT = olfactory tubercle; SI = substantia innominata; BNST = bed nucleus of the stria terminalis; MA = magnocellular nucleus; PVH = paraventricular hypothalamic nucleus; Hypothal. = hypothalamus; CeA = central amygdala; Thal. = thalamus; ZI = zona incerta; COA = cortical amygdalar area; MB = midbrain; Sup. = superior; PAG = periaqueductal gray; Inf. = inferior.

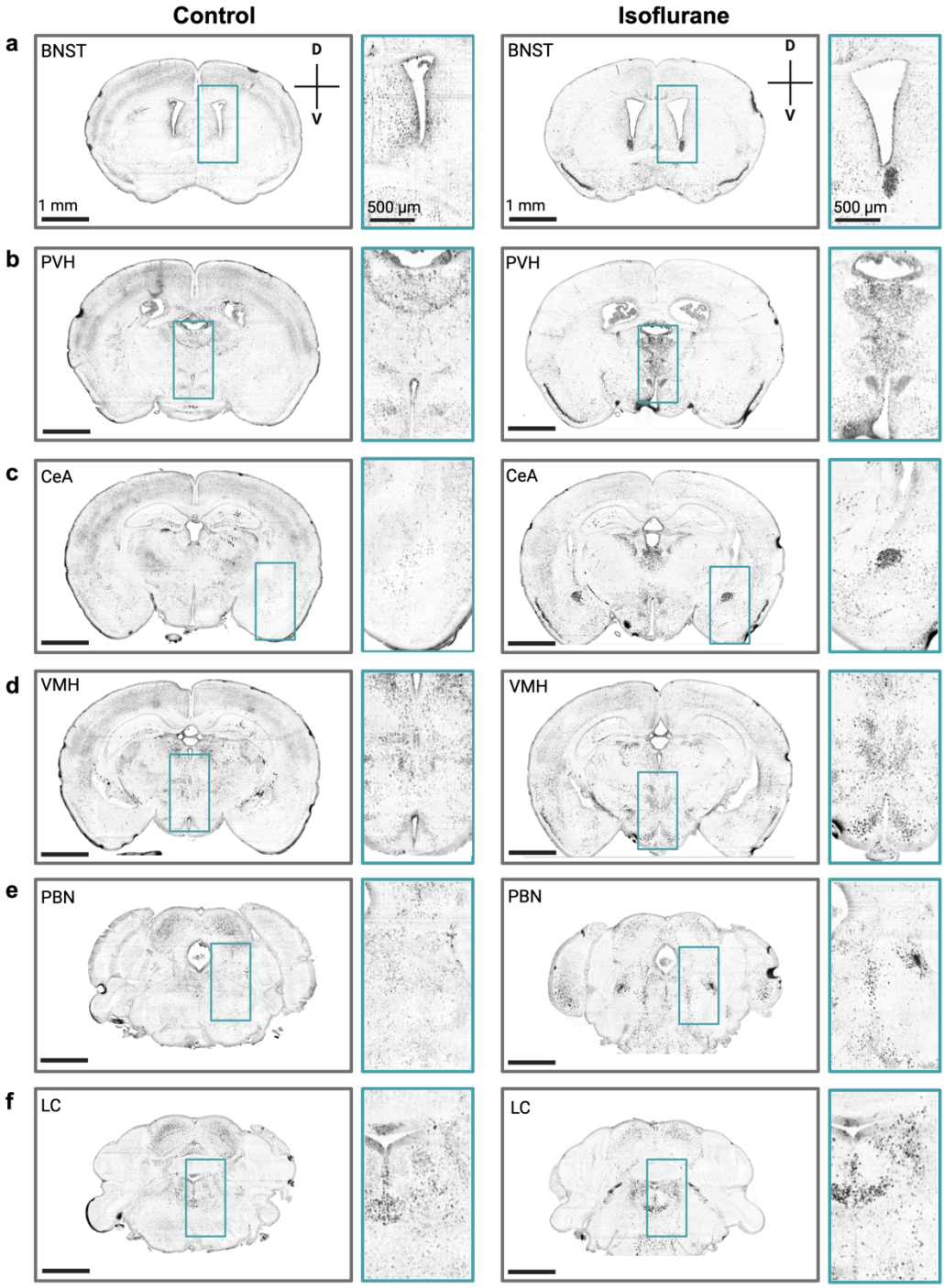

Extended Figure 6. Representative Fos immunolabeling from cleared intact brains. Images from a representative control (left column) and an isoflurane mouse (right column) from Figure 2. Images were acquired with a light sheet microscope using a 3.6X objective in the horizontal plane and then re-sliced to the coronal plane to identify (**a**) BNST = bed nucleus of the stria terminalis, (**b**) PVH = paraventricular hypothalamus, (**c**) CeA = central amygdala, (**d**) VMH = ventromedial hypothalamus, (**e**) PBN = parabrachial nucleus, (**f**) LC = locus coeruleus. Scale bars are 1mm for the full coronal slice and 500 µm for the inset image.

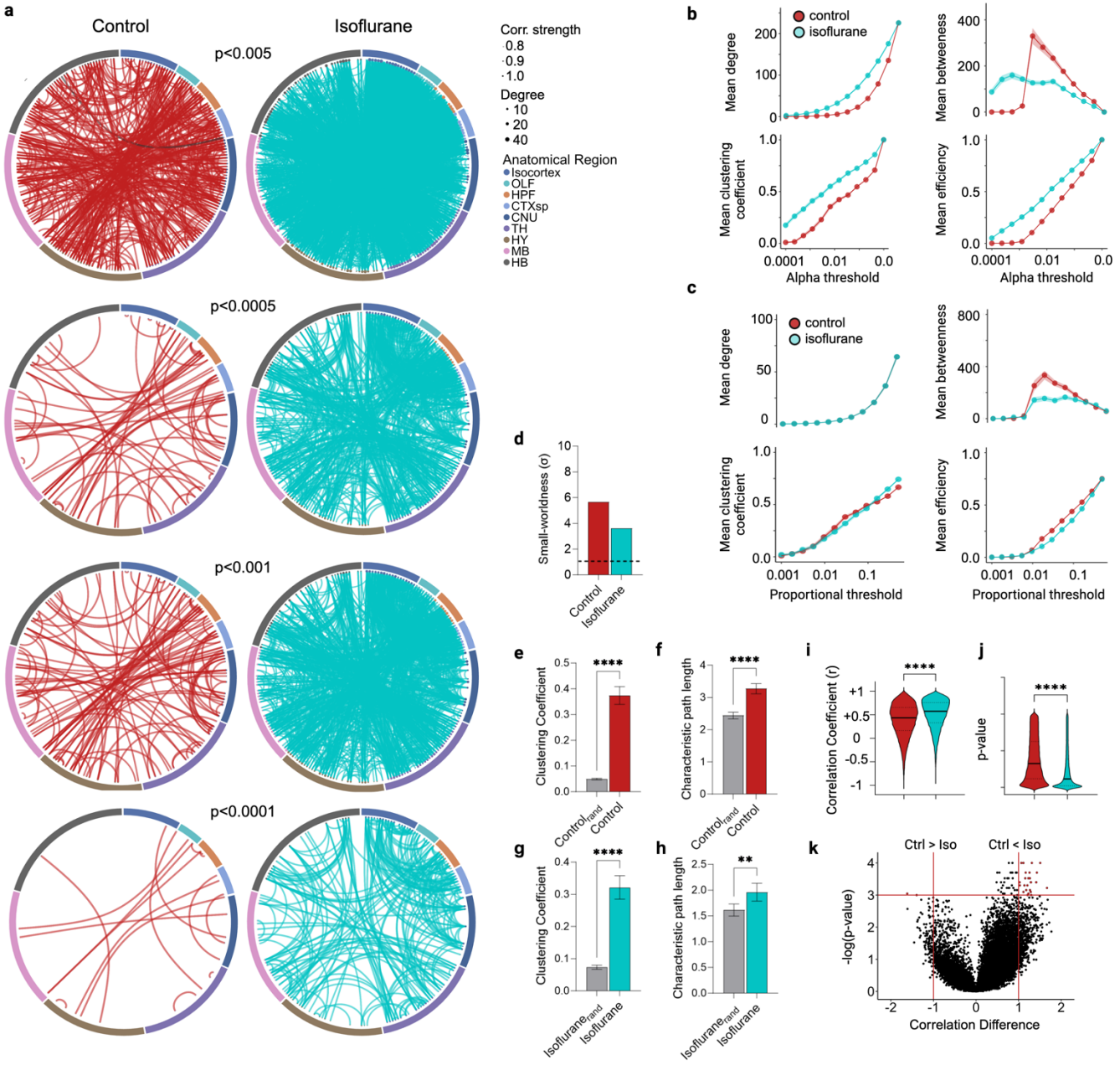

Extended Figure 7. Isoflurane networks are denser across a variety of weight thresholds. (**a**) control (red) and isoflurane (blue) networks thresholded at various alpha values. (**b**) Mean degree, clustering, betweenness, and efficiency metrics calculated across a range of significance thresholds and (**c**) edge proportion thresholds. (**d**) Assessment of small-world properties of individual networks plotted in Fig 3. Small-world index (σ) for both networks are above the threshold of 1 (black dotted horizontal line). The control network (**e**) clustering coefficient and (**f**) path length as well as the isoflurane (**g**) clustering coefficient and (**h**) path length are higher than randomly rewired networks with matching degree sequences. (**i**) Distributions of the Pearson correlation coefficients between all unique regional connections and their associated (**j**) p-value for the control and isoflurane networks. (**k**) Volcano plot illustrating the regional correlations which most differ between the networks. The horizontal red line denotes a significance threshold of $p < 0.001$. Red points in the upper right (control < isoflurane) and upper left quadrants (control > isoflurane), defined by vertical red line lines, indicate regional correlation differences with a magnitude shift greater than 1 between groups. Two-tailed Student's *t*-test: **p<0.01, ****p<0.0001. Error bars represent mean ± SEM. See Extended Data Tables 6-8 for full abbreviations and detailed statistics.

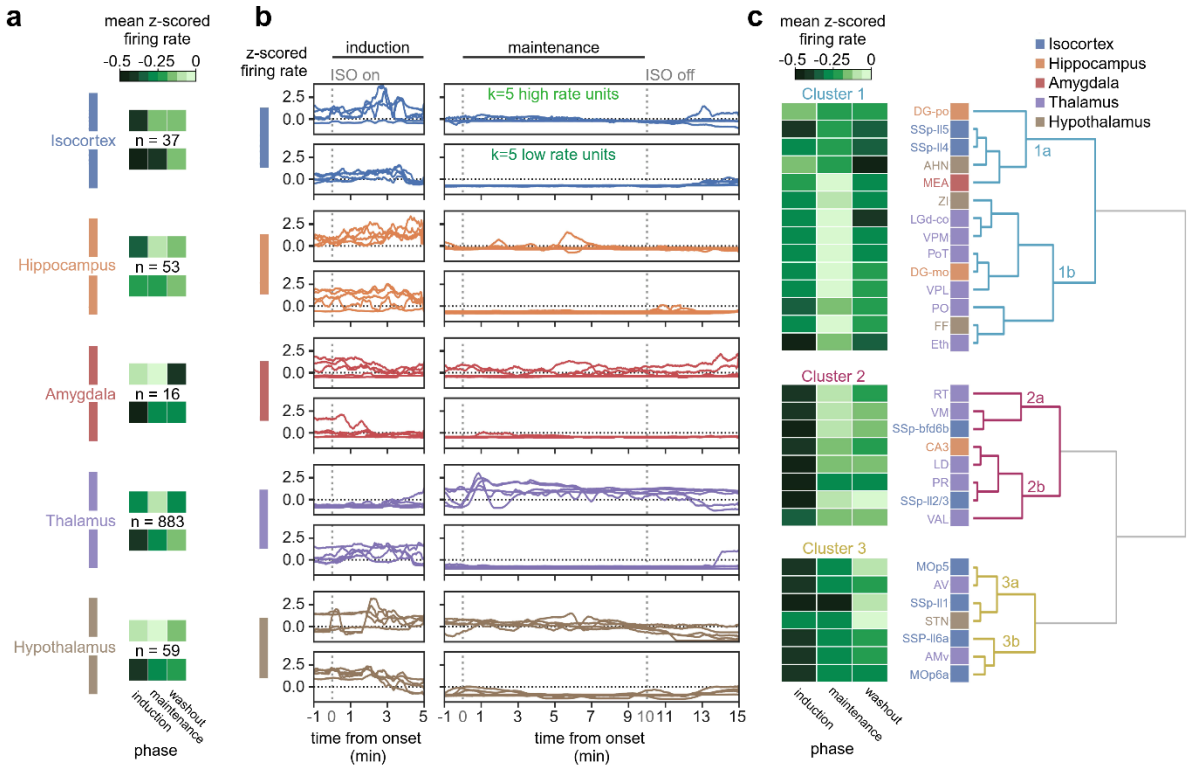

Extended Figure 8. Response variability during isoflurane. (**a**) Heatmaps showing mean normalized firing for each major region (isocortex, hippocampus, amygdala, thalamus, and hypothalamus) across anesthetic phases (induction, maintenance, washout) with the total unit counts (*n*) for each region. (**b**) Representative traces from units in major regions with diverse responses under isoflurane. For each major region, traces show 5 units (*k*=5 from total unit count *n* for each region) with the highest (top) and lowest (bottom) mean normalized firing during the maintenance phase. Left traces show 1 min prior and 5 min following onset of induction at the dashed line ("ISO on"). Right traces show 1 min prior and 10 min following onset of maintenance phase (first dashed line) and the "ISO off" time (right dashed line). (**c**) Mean z-scored firing from each experimental phase was clustered (Ward's method) for all subregions obtained in recordings. Hierarchical clustering of subpopulation means revealed 3 heterogeneous clusters (CHI=11.12), each with subclusters (e.g., 1a: Cluster 1a) linking spatially distributed cortical and subcortical structures. See Extended Tables 9 and 12 for detailed data.

Methods:

Mice. All experiments were approved by the National Institutes of Health and the University of Washington Institutional Animal Care and Use Committee. 3- to 6-month-old male and female c57bl/6j or homozygous Fos $^{2A\text{-}iCreER}$ (FosTRAP2) transgenic mice are used in all studies. Animals are group-housed in a 12-hour reverse light/dark cycle facility with ad libitum access to food and water. Animals used in electrocorticography or Neuropixels studies are singly housed during the recording experiments.

Intact brain tissue collection after isoflurane exposure: Mice were singly housed in the home cage for 3 days prior to tissue collection for intact whole brain Fos immunolabeling. Habituation to the testing room was achieved by placing mice in a temperature controlled red-light room for at least 2-3 hours a day for 3 days prior to tissue collection. On the test day, mice in the control condition remained singly housed in their home cage inside the testing room where isoflurane was delivered. Mice in the isoflurane condition were individually induced with 2% isoflurane and once loss of toe pinch reflex was confirmed, each mouse was maintained under general anesthesia for 180 minutes with 1.2%-1.3% isoflurane in oxygen delivered via nose cone. The concentration of isoflurane delivered at each nose cone was confirmed to be within range using a gas analyzer prior to placing the mouse in the nose cone. Mice were actively warmed on a heating pad and continuously monitored by the experimenter. After 180 minutes, all mice were more deeply anesthetized with isoflurane and transcardially perfused with PBS followed by 10% formalin. Brains were dissected and post-fixed in formalin for 24 hours at 4°C prior to intact whole brain immunolabeling and clearing.

Intact brain clearing and immunolabeling: A previously published, modified version of the iDisco+ protocol was used to immunolabel and clear intact brain samples[1,2]. The following antibodies were used: Synaptic Systems Rat anti-cFos (1:2000) for Fos immunolabeling or Rockland Rabbit anti-RFP (1:2000) for mCherry DREADD immunolabeling followed by Donkey anti-Rat or Donkey anti-Rabbit Jackson ImmunoResearch AlexaFluor 647 Fab2-conjugated secondary antibody (1:500).

Intact brain imaging: Cleared, intact whole brains were imaged with a uniform axial resolution light sheet microscope (SmartSPIM, LifeCanvas Technologies) using either the 1.6x (5 µm voxels) or 3.6x (1.8 µm voxel) objectives for Fos samples, and 3.6x for TRAP samples. Samples were mounted horizontally using a custom sample holder immersed in dibenzyl ether (DBE). Images were acquired in two channels (488 nm: autofluorescence; 639 nm: mCherry/AlexaFluor-647) and stitched using the SmartSPIM acquisition software. TRAP+ images were down-sampled (0.5x) prior to image processing with isotropic 3.6 µm voxels. 3-dimensional images were visualized using Arivis Pro software (Zeiss).

ClearMap brainwide TRAP+ analysis: We processed 7 intact formalin-fixed brain samples from FosTRAP2 transgenic mice infected with AAV-PHP.eB-DIO-Gq-DREADD-mCherry virus (see *Retroorbital virus injection* and *Activity-dependent labeling* procedures) using a modified version of the ClearMap pipeline as previously published[2,3]. We trained a pixel classifier in Ilastik to segment and quantify single cells based on somatic signal classification. This was achieved by selecting 21 image tiles (200 × 200 × 220 µm) from three separate samples, cropped from dorsal (2), central (3), and ventral (2) positions of the brain. To improve segmentation accuracy, an

additional three tiles were used to correct for artifacts in ventricular and boundary regions. The fully trained classifier was then applied to all samples, generating segmented cell counts per brain region and voxelized heatmaps. We computed TRAP+ cell counts within two different levels of hierarchy within the Unified Brain Atlas: 1) 11 major anatomical divisions (Extended Fig 3b) and 914 minor subregions within those high-level anatomical divisions that no longer split into further daughter regions. We provide the raw TRAP+ cell counts, cell density, and statistical results for all analysis (Extended Data Table 3).

ClearMap brainwide Fos analysis: We processed 16 intact brain samples (n=7 controls and n = 9 isoflurane) using a modified version of the ClearMap pipeline as previously published[2]. We computed Fos-positive activated cell counts within two different levels of hierarchy within the Unified Brain Atlas: 1) 11 major anatomical divisions (Extended Fig 4) and 914 minor subregions within those high-level anatomical divisions that no longer split into further daughter regions (Fig 2d). To ensure accuracy within the hierarchical relationships, we ensured there were no overlapping spatial footprints and no double counting of any regions, following each subregion branch until the end or "stop-level." We transformed the raw Fos cell counts to z-scores and normalized the data to account for regional volume differences. We used the home cage control group (control) to normalize the z-scores for each region of interest using the formula $z= (x-\mu)/\sigma$, where x represents the Fos count of the treatment group, μ represents the mean Fos count of the control group, and σ represents the SD of the control group. We then converted the z-score into -log10 for visualization. For the high-level analysis, we used an unpaired t-test, *$p<0.05$ (Extended Fig 4i). For the stop-level analysis, we used a t-test followed by the false discovery rate (FDR) multiple comparison correction with an alpha significance level of 0.01 ($q < 0.01$), two-tailed (Fig

2d). We provide the raw Fos counts, z-scored data and statistical results for all analysis (Extended Table 3).

UNRAVEL Fos analysis: We also analyzed whole brain Fos immunolabeling using UNRAVEL[4] (UN-biased high-Resolution Analysis and Validation of Ensembles using Light sheet images), with refactored Python code (documentation: b-heifets.github.io/UNRAVEL/index.html). Autofluorescence images were resampled to 50 μm resolution, and tissue was masked using Ilastik (v1.4.0; pixel classification; all features) for N4 bias field correction (ANTsPy; 0.4.2). The resampled images were padded (15% voxels on all sides) and smoothed with a Gaussian filter (sigma = 0.4) before being registered with an average template from iDisco and light-sheet microscopy (LSFM), which was aligned with the Allen Mouse Brain Common Coordinate Framework (CCFv3)[5]. Registration was performed using ANTsPy: ants.affine_initializer(fixed_image=autofluorescence_image, moving_image=template, search_factor=1, radian_fraction=1, local_search_iterations=500), followed by ants.registration(fixed=autofluorescence_image, moving=template_aligned_with_tissue, grad_step=0.1, syn_metric='CC', syn_sampling=2, reg_iterations=(100, 70, 50, 20)). Registration accuracy was visually confirmed using FSLeyes (v0.30.1; FMRIB), with the atlas warped to each fixed registration input image. Fos immunofluorescence was enhanced through 3x3x3 spatial averaging and rolling ball background subtraction (pixel radius = 4). The resulting images were warped to 25 μm atlas space using transforms from registration. Each hemisphere was z-scored using a warped tissue mask and a hemispheric mask ((image − mean intensity in the brain)/standard deviation of intensity in the brain). The images were smoothed with a 100 μm kernel and mirrored

to average the left and right sides. A unilateral atlas mask, excluding ventricles, fiber tracts, and undefined regions, spatially restricted the voxel-wise analyses.

Voxel-wise comparisons between the isoflurane and control groups (t-test design) were performed using non-parametric permutation testing (18,000 permutations) with the general linear model (randomise_parallel; FMRIB; v6.0.2). P-value maps were corrected for multiple comparisons using the false discovery rate (FDR) method, applied across a series of q-values to identify clusters of significant voxels. Data in Fig. 2 are from the most stringent q-value thresholds ($q < 0.005$, $p < 0.000056$ for Control < Isoflurane; $q < 0.05$, $p < 0.0012$ for Control > Isoflurane). Clusters smaller than 100 voxels were excluded. Clusters were warped back to full-resolution tissue space for cell density measurements (Fos+ cells per cluster volume). Fos+ cells were segmented using Ilastik. 3D counting was performed using connected components-3d (v3.16.0; connectivity = 6). Clusters were considered valid if unpaired t-tests confirmed that differences in Fos labeling reflected changes in Fos+ cell densities. Information on valid clusters, including regional composition and Fos+ cell densities across FDR q-values, is provided in Extended Table 5. Statistical maps and other related data are available upon request. Scripts from UNRAVEL (github.com/b-heifets/UNRAVEL) are available at zenodo.org/records/13655988.

Correlational, Permutation, and Network Analysis: All associated network analyses and visualizations were conducted with the SMARTTR[6] package, igraph, tidygraph package, and custom written functions. Pearson correlations between normalized Fos^+ activity per region were calculated and asymptotic p-values for each correlation were determined using a one-sample t-test. Significantly correlated regions are visualized in heatmaps after FDR (Benjamini-Hochberg)

115 correction using a significance threshold of $q < 0.05$. A permutation analysis was conducted to
116 identify the functional connections which differed most between experimental groups.
117 Correlations differences were calculated by subtracting correlations from the Control group from
118 respective correlations in the Isoflurane group ($r_{Isoflurane} - r_{Control}$). Each correlation difference was
119 used as a test statistic against a null distribution produce by shuffling the labels of Control and
120 Isoflurane mice 10,000 times, with the correlation difference recomputed for each shuffle. Each
121 test statistic was compared to its individual null distributions to determine the p-value. Significance
122 correlation differences for all analyses were thresholded using an alpha value of 0.001 and
123 visualized as constructed network. Edge thickness in the permuted network represented magnitude
124 of correlation difference, with regions represented as nodes. An agglomerative fast greedy
125 modularity optimization algorithm[2] was applied using tidygraph for community detection.

126 Individual functional networks for the Control and Isoflurane test conditions were
127 constructed by representing regions as nodes and Pearson correlation values as edges, with
128 correlation magnitude corresponding to edge thickness. Since pairwise correlations were
129 calculated for all pairs, the initial functional network is complete, with all nodes fully
130 interconnected. Thresholding is normally applied to assess the topological features of the most
131 salient connections, although there is little consensus on the best approach, (i.e., thresholding by
132 connection strength or connection proportion) or choice of threshold[3]. Thus, we constructed
133 networks for Control and Isoflurane across a range of alpha thresholds (FDR uncorrected) from
134 0.0001 to 1, and across a range of edge proportion thresholds, from 0.001 to 0.50.

135 In both the permuted and individual functional networks, several topology metrics per
136 node, such as degree, clustering coefficient, efficiency, and betweenness centrality[4] are
137 automatically calculated using the create_networks() or create_permutation_network() functions

in SMARTTR. Summary statistics are calculated using the summarise_networks() function, which averages nodal metrics to calculate mean degree, mean efficiency, mean clustering coefficient, and mean betweenness for a given network. To assess for "small-world" properties[5] of empirical Control and Isoflurane networks (edge proportion of 3.15%), we compared the clustering coefficient (C) and characteristic path length (L) with the corresponding values (C^{rand}, L^{rand}) averaged from 100 random null networks. Null networks are generated by applying the degree sequence-preserving maslov-sneppen[6] rewiring algorithm with the rewire_network() function, and averages metrics were calculated with summarize_null_networks(). Number of edge rewirings per random network are equivalent to number of edges x 100. The small-world index (s), a ratio summarizing the propensity for high clustering while maintaining efficiency in a network, is defined here as $\frac{C/C^{rand}}{L/L^{rand}}$. Values above 1 are considered indicative of small-world properties. All analysis code is available on (https://mjin1812.github.io/SMARTTR)

Head-fixed implantation and habituation: For high density silicon probe (Neuropixels) recordings, mice were implanted with a custom-made titanium headplate (H.E. Parmer Company, TN) for head-fixation of the animal, and 3D-printed "well"[7] providing safe access for probe insertion and retention of saline solution on the skull surface during recordings. Following recovery (~2 weeks), mice were habituated to head-fixation for at least 3 days, starting with 15- to 20-min periods and increasing daily by 20 min until they exhibited minimal distress with fixation for 1 h[8]. For head-fixed recordings, mice were placed in a 3D-printed mouse holder[9] adapted for isoflurane delivery via a 3D-printed stereotax anesthetic nose cone. During recordings, estimated isoflurane gas concentration was measured with a gas analyzer (BC Biomedical, MO).

High-density in vivo Neuropixels recordings: Male and female mice were prepared for head-fixed recordings in a behavioral rig adapted for isoflurane delivery and gas analyzer sampling at the nose cone. At least 1 day prior to each recording, craniotomies were made targeting regions of interest, planned beforehand using a specialized tool[10] to take into consideration optimal probe orientations and angles of entry (5-15°), and finally sealed with Kwik-Cast (World Precision Instruments, FL). When not sealed, craniotomies were kept moist with continuous applications of saline into the "well." On recording days, mice were first head-fixed and allowed to acclimate before probe insertion. Neuropixels 1.0 probes were mounted on a micromanipulator system (Sensapex, SC) and lowered via the planned trajectory to 100 µm beyond the target depth, then retracted after a 10-min delay and allowed to rest for an additional 10 min before starting the baseline recording. After a 5-min awake baseline, mice were induced with isoflurane to an initial target 1.5% concentration. Intermittent foot pinches were used to determine loss-of-reflex (LOR) time. Following LOR, mice were maintained at 1.3% isoflurane to begin the steady-state maintenance phase recording (Fig 4). After 10 min, the vaporizer was turned off for washout period of recording (Extended Fig 8). Mice were actively warmed via external heating pads. Each animal (n=4) had two recording sessions at least 24 hours apart, and one recording was left out due to poor signal quality for a total of 7 recording sessions. Altogether, we obtained units totaling N=1048; Isocortex, n=37; Hippocampus, n=53; Amygdala, n=16; Thalamus, n=883, Hypothalamus, n=59; see Extended Data Table 10. All recordings were acquired using SpikeGLX (Janelia Research Campus, VA).

Histological alignment of recording tracts: To determine the placement of isolated units in the brain, sorted units were aligned to the probe tracts after intact brain imaging. After recordings,

intact formalin-fixed brains were cleared and imaged with light sheet fluorescent microscopy for probe tract tracing in the Allen Brain Atlas space and mapped onto the locations of isolated units to identify their placement in the brain (Fig 4b and see *Intact brain clearing* and *imaging*). After registering each brain to the Allen CCF[11], probe tracts made by application of the lipophilic CM-DiI dye (Thermo Fisher, WA) to the probe shank before each recording were traced in Lasagna[12] to yield a fitted line of XYZ coordinates, which were visualized in Brainrender[11]. A separate open-source tool[13] was used to adjust the alignment of activity recorded along the shank to the regions identified along the tract.

Neuropixels data processing: Spike sorting was performed with Kilosort4[14], isolated units were discarded if they had fewer than 1000 spikes across the whole recording and filtered out further based on quality metrics assessment[15]. To prevent false negatives due to widely-observed prolonged inhibitions from anesthetic induction, units were primarily filtered out if they concurrently exhibited low presence and low firing rate (<0.5 Hz), or a poor score on *L-ratio* or *D-prime* isolation metrics[16,17]. Remaining units were inspected manually using Phy[14]. Postprocessing and curation was performed using custom scripts integrating open-source Python packages[18].

Neuropixels data analysis: Spike times were binned into 250-ms bins and averaged to yield each unit's mean firing rates. For representative isoflurane activity traces, normalized firing rates were calculated by first subtracting the mean firing during the last 2 min of the baseline phase, then z-scored across the whole recording. For mean region and subregion activity heatmaps, firing rates were z-scored across the recording. Mean rates during "induction," "maintenance" or "washout"

phases were taken across all units in each major region or subregion (Extended Fig 8). Cortical and subcortical subregion normalized firing rates were averaged and compared via one-way ANOVA. For k-means clustering, subregion normalized firing rates were used as features for the elbow method analysis, yielding an optimal grouping of 6 clusters with asymptotic inertia and silhouette scores. All analyses were conducted using custom Python scripts integrating open-source packages.

Retroorbital virus injection: FosTRAP2 mice were briefly anesthetized with isoflurane (5-10-min) and administered adeno-associated virus (AAV) by retroorbital injection to one eye. AAV-PHP.eB-hSyn-DIO-hM3D(Gq)-mCherry (44361-PHPeB, Addgene) was used for activating DREADD and AAV-PHP.eB-hSyn-DIO-hM4D(Gi)-mCherry (44362-PHPeB, Addgene) was used for inhibitory DREADD. Virus was diluted in total 100µL sterile saline to ~ 2-3x10^{11} GC/mL based on prior studies[19].

Activity-dependent labeling (TRAP): 3-4 weeks following retroorbital virus injection, FosTRAP2 mice were induced with 2% isoflurane and then maintained unresponsive at 1.2-1.3% for a total time of 180 min. Mice were actively warmed on a heating pad and continuously monitored by an experimenter. A single 50 mg/kg intraperitoneal (i.p.) injection of 4-hydroxytamoxifen (4-OHT, Sigma Aldrich), was administered at the 90-min halfway point during the isoflurane exposure to induce *Cre*-recombination and activity-dependent labeling[20]. Non-TRAP control mice also received retroorbital virus injections and isoflurane exposure but then sesame oil vehicle (Sigma Aldrich) in the equivalent volume of 4-OHT (~0.2mL) was given i.p. at the 90-min halfway point.

Clozapine-n-oxide administration: Clozapine-n-oxide (CNO, Enzo Life Sciences) was solubilized in water and stored as 5mg/mL aliquots. For testing, the aliquot was diluted in sterile saline to an end concentration of 0.5 mg/mL for 5 mg/kg behavioral studies. Mice received i.p. injections according to their body weight ranging from 0.2-0.3 mL for a 20-30g mouse. The equivalent volume i.p. sterile saline was delivered for saline trials.

Electrocorticography surgical procedure & neural signal data recording: Electrocorticography (ECoG) was recorded using a tethered implant as previously described[27]. Briefly, using aseptic stereotaxic surgical techniques under isoflurane anesthesia, a midline incision was made above the skull, and ECoG-recording electrodes (Pinnacle Technology, Lawrence, KS; No. 8209: 0.10-in.) were screwed through cranial holes at the following coordinates:

- *Channel 1 (left frontal cortex)*: 1.5 mm lateral and 2 mm anterior to bregma
- *Channel 2 (right parietal cortex)*: 1.5 mm lateral and 2 mm posterior to bregma
- *Ground (visual cortex)*: 1.5 mm lateral and 4 mm posterior to bregma
- *Reference (cerebellum)*: 1.5 mm lateral and 6 mm posterior to bregma

Mice were singly housed in standard cages under a 12:12 light-dark (LD) cycle following surgery. After a 14-day recovery period, they were moved to recording cages, fitted with a tether and preamplifier (100x signal gain) connected to the Pinnacle Technology recording system, and given at least 1 day to acclimate before recording.

Animals were injected with saline or CNO (5mg/kg) at the same time of day on consecutive days (days 1 and 2, respectively), with pre-experimental (day 0) and post-experimental (day 3) days serving as baseline comparisons. To assess neural dynamics during isoflurane, mice were placed in a specialized chamber and induced with 3% isoflurane until fully immobile (~10

minutes). Isoflurane was then discontinued, and the mice were allowed to fully wake (~20–30 minutes). In all recording days, electromyography (EMG) signals were obtained by inserting a pair of silver wires into the neck muscles. All screws and wires were connected to a common 6-pin connector compatible with the Pinnacle recording device using silver wire. Signals were continuously recorded at 400 Hz with low-pass filters at 100 Hz. All recordings were saved and exported for processing using the European Data Format (EDF). Simultaneously, animal activity was continuously recorded using webcams.

For each animal, one hour of data (time-matched across days) was extracted for each condition (pre, saline, CNO, post), along with the entirety of the isoflurane induction condition, and saved to individual .edf files. Spectrograms were generated by low-pass filtering each file at 12 Hz and log-transforming the signal data. Additionally, slow wave signal-to-noise ratio (SNR) was calculated using minute-long bins by dividing mean power in the delta frequency band (1–4 Hz, primarily capturing delta waves associated with sleep and anesthesia[28]) by mean power in surrounding frequencies (0.5–1 Hz + 4–7 Hz). All analyses were conducted using the left frontal cortex electrode (i.e., channel 1).

To quantify the change in delta (1-4 Hz) over the course of drug onset (i.e., 1 minute prior to and 15 minutes following drug onset), we ran a linear mixed model predicting delta activity ratio using the interaction term *time* × *condition* (using the 'Pre' condition as reference and controlling for the random effect of individual animal). The results show that the only significant differences in delta activity were the increases seen over time in the CNO and ISO conditions, with no other significant direct or interaction effects (see Extended Data Table 1).

Open field test: CNO dose-dependent changes in maximum velocity were assessed in a 30 x 30 cm open field chamber (Extended Fig 1c-d). Mice were habituated to the chamber for at least 3 days. On alternating days, they received intraperitoneal injection of either 1 mg/kg CNO, 5mg/kg CNO, or the equivalent volume of saline, and were placed in the box for 20-min with concurrent webcam video recording. A total of 3-4 trials per drug condition from 6 Gq-DREADD-expressing mice and 5 Gi-DREADD expressing mice were analyzed for changes in movement velocity using Any-MAZE video tracking software. GraphPad Prism was used to analyze data with 2-way ANOVA and Tukey multiple comparison post-tests. See Extended Data Table 1 for statistics.

Loss of righting reflex: Latency to loss of righting reflex was assessed in a chamber equipped for isoflurane delivery and sampling of isoflurane concentration with a gas analyzer (Extended Fig 1a). Mice were individually injected with 10 mg/kg CNO or saline in alternating trials at least one day apart and placed in the chamber. Isoflurane was administered stepwise from 0.5 to 2% on the vaporizer in 0.5 increments and loss of righting reflex was assessed at each stepwise increment with the exact sampled concentration recorded.

Warm water tail withdrawal test: Mice were tested for the latency to remove their tail from a warm water bath (52.5°C). Mice are restrained within a paper towel, and 1/3 to ½ of the tail is immersed, and the time to remove the tail (tail flick latency) is recorded[22–25]. This is done at baseline after saline, and then in 30-min intervals after CNO injection. See Extended Data Table 1 for statistics.

Hot plate test: Mice are placed on a 53°C plate for 30 seconds, and behaviors are video recorded[26]. This occurs at baseline and after CNO at 2-time intervals (30-min and 90-min post-CNO)

298 interleaved between tail withdrawal tests. Latency to jump, groom paws, and number of
299 occurrences for these behaviors are quantified from videos by two independent researchers. See
300 Extended Data Table 1 for statistics.
301
302 *Rotarod test:* Coordination post CNO injection was tested for each mouse on a rotarod after
303 modified open field testing (Fig 1b and Extended Fig 1b). Mice were habituated for two days, 10-
304 min per day, at 4 rotations per minute (rpm) before testing. On test day, mice received a saline i.p.
305 injection in the morning and were placed on the rotarod at 4 rpm. Latency to fall was recorded,
306 unless animals stayed on for the duration of the experiment (10 min). Mice were recorded again in
307 the afternoon with a 5mg/kg i.p. CNO injection. See Extended Data Table 1.
308
309 *Wireless mechano-acoustic device implant:* Mice were implanted with wireless mechano-acoustic
310 devices (MA device: nVital, NeuroLux, Inc.) subcutaneously on the ventral surface while under
311 isoflurane anesthesia for a duration of less than 30 min. They were then group housed following
312 surgery. See Ouyang et al.[21] for surgical procedure and device details.
313
314 *Modified open field test and MA device data collection:* For 3 days before the experiment, mice
315 were habituated to saline intraperitoneal (i.p.) injections and explored a 15cm x 15cm smaller,
316 modified open field box for 10 min. The sides of the box were wrapped in 14G copper wire
317 attached to tuner and power distribution control (PDC) boxes (NeuroLux, Inc). Implanted wireless
318 mechano-acoustic (MA) devices were also tested during this time along with power input from the
319 PDC box (7 watts). During each experiment day, the animal explored the enclosure for 2-min
320 before an i.p. injection of either saline or 5mg/kg clozapine-n oxide (CNO, Enzo Life Sciences).

Recordings were taken with a web-camera positioned directly above the animal for 20-min. During each CNO trial, the first observable loss of mobility was documented as "drug onset." The average latency to immobility in all CNO trials was used to time-align "drug onset" in saline trials. Each mouse underwent 3 saline trials and 2-3 CNO trials over 6 days with no more than one trial per day. A total of 18 CNO trials and 20 saline trials was analyzed from 7 Gq+ mice (3 females, 4 males) in Fig 1. A total of 17 CNO trials and 17 saline trials was analyzed from 6 Gi+ mice (2 females, 4 males) in Extended Fig 1. Behaviors for a sub-selection of animals were manually scored to identify commonly observed behaviors, as well as determine criteria for behavioral classifiers. Video recordings collected during the experiment were used for pose estimation and supervised behavioral analysis (see *Modified open field test behavioral analysis)*. Data collected from the MA devices were processed with custom Python scripts. GraphPad Prism was used to analyze group means and paired t-tests. See Extended Data Table 1 for statistics.

Perfusion for tissue processing: After all studies, mice were deeply anesthetized with isoflurane and underwent transcardial perfusion with phosphate-buffered saline (PBS) followed by 10% formalin and dissection of the brain for further analysis (see *Intact brain clearing and immunolabeling)*.

Modified open field test behavioral analysis: We created pose estimation models to track 9 body-part key-points using SLEAP[6] (snout, left ear, right ear, left lateral, right lateral, centroid, tail base, tail center, and tail-tip). Missing pose-estimation data was interpolated using forward fill and the data was smoothed using a Savitsky-Golay filter across a 500ms sliding window. Grooming, rearing, and Straub tail were detected using random forest classifiers[29]. Freezing and circling were detected using heuristic rules as previously described[30,31].

345

346 *Annotation*: Behavior was annotated in 20-min video clips obtained from the modified open field
347 test. For fitting the Straub tail classifier, we used a sampled annotated dataset where the behavior
348 was present in 24244 frames (808s) and behavior was absent in 627312 frames (20910s). For fitting
349 the grooming classifier, we used a sampled annotated dataset where the behavior was present in
350 47005 frames (1566s) and behavior absent in 94010 frames (3133s). For fitting the rearing
351 classifier, we used a sampled annotated dataset where the behavior was present 31596 frames
352 (1053s) and behavior absent in 315960 frames (10530s).

353

354 *Featurization:* We featurized video and pose-estimation data using image, movement, geometry,
355 circular- and frequentist statistical methods (see below). For acceptable runtimes, we used GPU
356 accelerated and multiprocessing methods available through the SimBA API[29] . Features were
357 computed in metric space after calculating the pixel-to-metric conversion factors in the SimBA
358 graphical interface. Classifications were smoothened to remove any detected bouts less than
359 200ms in length. Computations are primarily dependent on numba[32] and shapely[33] libraries and
360 the featurization classes are available on the SimBA GitHub repository.

361

362 *Grooming and rearing behavioral classifiers:* We used the same feature set to create classifiers
363 for rearing and grooming. This feature set included movement and acceleration measures of
364 individual body-parts as well as paired body-part movement Spearman correlations in sliding time
365 windows (0.25-2s). We also computed distribution descriptive statistics (mean, variance, sum, z-
366 scores, skew, median absolute deviations, mean absolute change, root mean square) of the animal
367 hull geometry and animal hull sub-geometries (animal hull width, length, and area, as well as head

area, posterior hull area, anterior hull area, left lateral hull area, right lateral hull area) in sliding windows of 0.25-2s. We computed Spearman correlations between the hull sub-geometry areas in the same sized sliding time-windows. Using circular statistics, we calculated descriptive statistics of animal directions including animal circular range, animal circular standard deviation, and directional vector lengths in sliding windows of 0.25-2s.

Straub tail classifier: For accurate Straub tail segmentation, we first performed video background subtraction and centered and egocentrically aligned the mice in the videos. Next, we defined a buffered (1.75cm in each direction) polygonal geometry using the mouse tail key-points (tail-base, tail center, tail-tip) and sliced the tail geometry from each frame. Using the tail geometry coordinates, we computed the tail geometry mean area, standard deviation, mean absolute deviation in sliding time-windows of 1-2s. For each frame, we compared the tail geometry to the tail geometry 0.5-2s seconds prior using Hausdorff distances. For the sliced images of the tails, we compared the current tail image versus the tail image 0.5-2s prior using mean squared error of the raw RGB pixel values. We also computed descriptive statistics (average, variance, sum, mean absolute change) of the tail tip and tail center movements, and the tail length in sliding windows of 1-2s.

Feature importance: Model Gini feature importance scores showed the following key feature determinants for each behavior: (1) *Grooming* was primarily influenced by features describing the distribution of the animal's head area, body length, and snout movement within sliding temporal windows. (2) *Rearing* was primarily driven by features capturing the distribution of the distance between the animal's ears, head area, and body width in sliding temporal windows. (3) *Straub tail*

was mainly determined by features describing the distribution of the tail-tip movements, tail length and area, overall body area and right-side hull area, as well as correlations between the movements of the tail tip and tail base in sliding temporal windows. See Extended Data Table 2 for detailed feature importance.

Performance: Out-of-sample frame wise performance showed strong performance for grooming (precision: 0.92, recall: 0.99, f1: 0.96), rearing, (precision: 0.98, recall: 0.96, f1: 0.97) and Straub tail (precision: 0.99, recall: 0.96, f1: 0.98). See Extended Data Table 2 for model metrics.

Heuristic models: Freezing and circling were detected using heuristic rules as previously described. Circling was scored as present when the directional circular range of the animal was above 320 degrees, and the animal movement (computed from the animal centroid key-point) was above 6cm in the preceding 10s time-window. Freezing was scored as present in frames where the velocity (computed from the mean movement of the nape, snout, and tail-base body-parts) fell below 5 mm/s in the preceding 3s. Although the nape body-part was not pose-estimated, this body-part was inferred as halfway between the two ears.

Methods References:

1. Renier, N. *et al.* Mapping of Brain Activity by Automated Volume Analysis of Immediate Early Genes. *Cell* **165**, 1789–1802 (2016).
2. Madangopal, R. *et al.* Incubation of palatable food craving is associated with brain-wide neuronal activation in mice. *Proceedings of the National Academy of Sciences* **119**, e2209382119 (2022).

3. Szelenyi, E. R. *et al.* An arginine-rich nuclear localization signal (ArgiNLS) strategy for streamlined image segmentation of single cells. *Proceedings of the National Academy of Sciences* **121**, e2320250121 (2024).
4. Rijsketic, D. R. *et al.* UNRAVELing the synergistic effects of psilocybin and environment on brain-wide immediate early gene expression in mice. *Neuropsychopharmacol.* **48**, 1798–1807 (2023).
5. Perens, J. *et al.* An Optimized Mouse Brain Atlas for Automated Mapping and Quantification of Neuronal Activity Using iDISCO+ and Light Sheet Fluorescence Microscopy. *Neuroinformatics* **19**, 433–446 (2021).
6. Jin, M. *et al.* A SMARTR workflow for multi-ensemble atlas mapping and brain-wide network analysis. 2024.07.12.603299 Preprint at https://doi.org/10.1101/2024.07.12.603299 (2024).
7. International Brain Laboratory. Behavior: Appendix 1: IBL protocol for headbar implant surgery in mice. 10437384 Bytes (2020) doi:10.6084/M9.FIGSHARE.11634726.V4.
8. International Brain Laboratory. Behavior: Appendix 2: IBL protocol for mice training. 2735505 Bytes (2020) doi:10.6084/M9.FIGSHARE.11634729.V3.
9. International Brain Laboratory. Behavior: Appendix 3: IBL protocol for setting up the behavioral training rig. 33751033 Bytes (2021) doi:10.6084/M9.FIGSHARE.11634732.V6.
10. Birman, D. *et al.* Pinpoint: trajectory planning for multi-probe electrophysiology and injections in an interactive web-based 3D environment. 2023.07.14.548952 Preprint at https://doi.org/10.1101/2023.07.14.548952 (2023).
11. Tyson, A. L. *et al.* Accurate determination of marker location within whole-brain microscopy images. *Sci Rep* **12**, 867 (2022).

12. Campbell, R., Blot, A., Crousseau & Winter, O. SainsburyWellcomeCentre/lasagna: Stable IBL. Zenodo https://doi.org/10.5281/ZENODO.3941894 (2020).
13. Faulkner, M. Ephys Atlas GUI. https://github.com/int-brain-lab/iblapps/tree/master/atlaselectrophysiology. (2020).
14. Pachitariu, M., Sridhar, S., Pennington, J. & Stringer, C. Spike sorting with Kilosort4. *Nat Methods* **21**, 914–921 (2024).
15. International Brain Laboratory *et al.* Spike sorting pipeline for the International Brain Laboratory. (2022).
16. Hill, D. N., Mehta, S. B. & Kleinfeld, D. Quality Metrics to Accompany Spike Sorting of Extracellular Signals. *Journal of Neuroscience* **31**, 8699–8705 (2011).
17. Schmitzer-Torbert, N. & Redish, A. D. Neuronal activity in the rodent dorsal striatum in sequential navigation: separation of spatial and reward responses on the multiple T task. *J Neurophysiol* **91**, 2259–2272 (2004).
18. Buccino, A. P. *et al.* SpikeInterface, a unified framework for spike sorting. *eLife* **9**, e61834 (2020).
19. Chan, K. Y. *et al.* Engineered AAVs for efficient noninvasive gene delivery to the central and peripheral nervous systems. *Nat Neurosci* **20**, 1172–1179 (2017).
20. DeNardo, L. A. *et al.* Temporal evolution of cortical ensembles promoting remote memory retrieval. *Nat. Neurosci.* **22**, 460–469 (2019).
21. Ouyang, W. *et al.* An implantable device for wireless monitoring of diverse physio-behavioral characteristics in freely behaving small animals and interacting groups. *Neuron* (2024) doi:10.1016/j.neuron.2024.02.020.

22. English, A. *et al.* A preclinical model of THC edibles that produces high-dose cannabimimetic responses. *eLife* **12**, RP89867 (2024).

23. Abraham, A. D. *et al.* Estrogen Regulation of GRK2 Inactivates Kappa Opioid Receptor Signaling Mediating Analgesia, But Not Aversion. *J Neurosci* **38**, 8031–8043 (2018).

24. Chavkin, C., Cohen, J. H. & Land, B. B. Repeated Administration of Norbinaltorphimine Produces Cumulative Kappa Opioid Receptor Inactivation. *Front Pharmacol* **10**, 88 (2019).

25. Schattauer, S. S. *et al.* Peroxiredoxin 6 mediates Gαi protein-coupled receptor inactivation by cJun kinase. *Nat Commun* **8**, 743 (2017).

26. Abraham, A. D. *et al.* Orally consumed cannabinoids provide long-lasting relief of allodynia in a mouse model of chronic neuropathic pain. *Neuropsychopharmacology* **45**, 1105–1114 (2020).

27. Hsu, Y.-W. A. *et al.* The dorsal medial habenula minimally impacts circadian regulation of locomotor activity and sleep. *Journal of biological rhythms* **32**, 444–455 (2017).

28. Amzica, F. & Steriade, M. Electrophysiological correlates of sleep delta waves. *Electroencephalogr Clin Neurophysiol* **107**, 69–83 (1998).

29. Goodwin, N. L. *et al.* Simple Behavioral Analysis (SimBA) as a platform for explainable machine learning in behavioral neuroscience. *Nat Neurosci* **27**, 1411–1424 (2024).

30. Sabnis, G. *et al.* Visual detection of seizures in mice using supervised machine learning. 2024.05.29.596520 Preprint at https://doi.org/10.1101/2024.05.29.596520 (2024).

31. Lopez, G. C. *et al.* Region-specific Nucleus Accumbens Dopamine Signals Encode Distinct Aspects of Avoidance Learning. 2024.08.28.610149 Preprint at https://doi.org/10.1101/2024.08.28.610149 (2024).

481 32. Lam, S. K., Pitrou, A. & Seibert, S. Numba: a LLVM-based Python JIT compiler. in
482 *Proceedings of the Second Workshop on the LLVM Compiler Infrastructure in HPC* 1–6
483 (Association for Computing Machinery, New York, NY, USA, 2015).
484 doi:10.1145/2833157.2833162.
485 33. Gillies, S. *et al.* Shapely. Zenodo https://doi.org/10.5281/zenodo.13345370 (2024).
486